

RICE UNIVERSITY

Upgrade Studies for the CMS Detector Muon  
System at the CERN LHC

by

Benjamin Ari Michlin

A THESIS SUBMITTED  
IN PARTIAL FULFILLMENT OF THE  
REQUIREMENTS FOR THE DEGREE

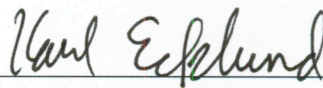
Master of Science

APPROVED, THESIS COMMITTEE:



---

Paul Padley, Chair  
Professor of Physics and Astronomy



---

Karl Ecklund  
Assistant Professor of Physics and  
Astronomy



---

Frank Toffoletto  
Professor of Physics and Astronomy

Houston, Texas

October, 2014

## ABSTRACT

Upgrade Studies for the CMS Detector Muon System at the CERN LHC

by

Benjamin Ari Michlin

In the upgraded Large Hadron Collider (LHC) environment the energy and luminosity will approximately double, and the Level-1 trigger (L1) rate will increase six-fold. This increase cannot be accommodated using current methods at the Compact Muon Solenoid (CMS) detector. Also, increased levels of ionizing radiation may interfere with muon endcap electronics. Unreliable performance of the L1 and endcap electronics can compromise physics studies. To determine if the upgraded electronics will function in the improved LHC environment, an irradiation study of the upgraded Muon Port Card (MPC) is performed. Additionally, Global Muon Trigger (GMT) muon isolation using the upgraded Muon Sorter (MS) is presented to reduce the L1 rate. It is determined that the upgraded MPC will operate properly, and that GMT muon isolation alone is not a viable method of rate reduction. Therefore, the MPC upgrade and GMT muon isolation will be implemented in the upgraded CMS detector.

## Acknowledgments

I would like to thank my advisor, Dr. Paul Padley, for all of his guidance, support, and wisdom. I would also like to express my gratitude to Dr. Karl Ecklund and Dr. Frank Toffoletto for their input and encouragement. Further, I would like to show my appreciation to Dr. Jabus Roberts and Dr. Mikhail Matveev for incorporating me into the radiation study discussed in Chapter 4, and Dr. Jamal Rorie and Dr. Laria Redjimi for all of their advice. Additionally, I would like to acknowledge Dr. Hannes Sakulin, Dr. Ivan Furic, and Joschka Lingemann for their counsel concerning GMT muon isolation detailed in Chapter 3. Finally, I would like to thank my family. Especially, my fiancée Taiana Vieira (who now likely knows more about physics than any other CPA), my sisters for actually reading my thesis, my dad, and my mom.

# Contents

Abstract	ii
Acknowledgments	iii
List of Figures	vii
List of Tables	ix
List of Acronyms and Initialisms	x
<b>1 Introduction and Motivation</b>	<b>1</b>
1.1 Introduction to Particle Physics and the Standard Model . . . . .	1
1.2 Motivation for Further Study . . . . .	4
1.3 Physics Motivation of the LHC and CMS Upgrades . . . . .	4
<b>2 The CMS Detector and its Upgrade</b>	<b>8</b>
2.1 Upgraded LHC Environment . . . . .	9
2.2 Upgrade of the CMS Detector . . . . .	11
2.2.1 Tracking System . . . . .	11
2.2.2 Limits on Tracking Precision . . . . .	13
2.2.3 Calorimeter System . . . . .	14
2.2.3.1 The Electromagnetic Calorimeter . . . . .	14
2.2.3.2 The Hadronic Calorimeter . . . . .	15
2.2.4 The Muon System . . . . .	16
2.2.4.1 Cathode Strip Chambers . . . . .	16
2.2.4.2 Drift Tubes . . . . .	24
2.2.4.3 Resistive Plate Chambers . . . . .	26
2.2.5 L1 Trigger Upgrade . . . . .	27

<b>3</b>	<b>GMT Muon Isolation</b>	<b>30</b>
3.1	Physics After LS1 . . . . .	31
3.2	Muon Production and Isolation . . . . .	32
3.3	Data . . . . .	35
3.4	Emulation . . . . .	36
3.4.1	HCAL . . . . .	37
3.4.1.1	Geometry and Segmentation . . . . .	37
3.4.1.2	Emulated $E_T$ vs HCAL Data Comparison . . . . .	39
3.4.2	ECAL . . . . .	43
3.4.2.1	Emulated $E_T$ ECAL Data Comparison . . . . .	43
3.5	RCT Region Map . . . . .	45
3.6	Selection Criteria and Variable Definitions . . . . .	48
3.6.1	Relative Efficiency . . . . .	48
3.6.2	Relative Rate . . . . .	52
3.6.3	Absolute Isolation Variable . . . . .	53
3.6.4	Relative Isolation Variable . . . . .	54
3.7	Results of GMT Muon Isolation . . . . .	57
3.7.1	Explanation of Endcap Behavior . . . . .	65
3.7.2	Effects of Isolation on Efficiency ( $ \eta  \leq 2.1$ ) . . . . .	67
3.7.3	Effects of Isolation on Efficiency in Endcap ( $1.2 <  \eta  \leq 2.1$ ) . . . . .	71
3.8	Summary . . . . .	74
<b>4</b>	<b>Radiation Testing of the Spartan-6 Programmable De-</b>	
	<b>vice for the CSC Upgrade</b>	<b>76</b>
4.1	Introduction . . . . .	77
4.2	Effects of Radiation on Electronics . . . . .	80
4.2.1	SEUs . . . . .	80
4.2.2	Permanent Damage . . . . .	81

4.3	Radiation Testing Setup . . . . .	81
4.4	Results . . . . .	82
4.5	Summary . . . . .	85
<b>5</b>	<b>Conclusions and Discussion</b>	<b>86</b>
5.1	Conclusions . . . . .	86
5.2	Future Work . . . . .	87
	<b>References</b>	<b>89</b>

# Figures

1.1	The Elementary Particles . . . . .	2
2.1	The CMS Detector . . . . .	9
2.2	Integrated Luminosity . . . . .	10
2.3	The Pixel Detector . . . . .	12
2.4	The Muon System . . . . .	17
2.5	CSC Layout . . . . .	18
2.6	Incident Muon on a CSC . . . . .	19
2.7	CSC Comparator Muon Reconstruction . . . . .	21
2.8	CSC Data Flow . . . . .	23
2.9	Detailed Diagram of ME1 . . . . .	25
2.10	Incident Muon on a DT . . . . .	26
2.11	Resistive Plate Chambers . . . . .	27
3.1	Dimuon Invariant Mass Spectrum and Hadronic Muon Rate . . . . .	33
3.2	Isolation Region Possibilities . . . . .	35
3.3	HCAL Geometry and Segmentation . . . . .	38
3.4	Artificial HCAL Tower Segmentation . . . . .	38
3.5	Online/Offline HCAL $E_T$ Comparison . . . . .	41
3.6	Online/Offline HCAL $E_T$ Comparison by Calorimeter Region . . . . .	42
3.7	ECAL Geometry and Segmentation . . . . .	43
3.8	Online/Offline ECAL $E_T$ Comparison . . . . .	45

3.9	RCT Region Map . . . . .	46
3.10	Online/Offline 3x3 RCT Region $E_T$ Comparison . . . . .	47
3.11	Efficiency Without Isolation . . . . .	51
3.12	Absolute Isolation Variable . . . . .	54
3.13	Relative Isolation Variable . . . . .	56
3.14	ROC: Relative & Absolute Isolation, Varying Full Granularity Region Radius . . . . .	58
3.15	ROC: Relative Isolation, RCT/Full Granularity Comparison . . . . .	59
3.16	ROC: Relative Isolation, Full Granularity, Varying $p_T^{GMT}$ Trigger $p_T$ Threshold . . . . .	62
3.17	ROC: Relative Isolation, Full Granularity, Varying $p_T^{GMT}$ Trigger $p_T$ Threshold and Resolution . . . . .	63
3.18	ROC: Relative Isolation, Full Granularity, Varying $p_T$ Resolution . . . . .	64
3.19	$p_T$ Distributions of Muons With and Without Isolation . . . . .	66
3.20	$p_T^{SA}$ Residual . . . . .	67
3.21	Efficiency with Relative Isolation ( $p_T^{GMT}$ ) . . . . .	68
3.22	Efficiency with Relative Isolation ( $p_T^{SA}$ ) . . . . .	69
3.23	Efficiency with Absolute Isolation ( $p_T^{GMT}$ ) . . . . .	69
3.24	Efficiency with Absolute Isolation ( $p_T^{SA}$ ) . . . . .	70
3.25	Efficiency with Relative Isolation ( $p_T^{GMT}$ , $1.2 <  \eta  \leq 2.1$ ) . . . . .	72
3.26	Efficiency with Relative Isolation ( $p_T^{SA}$ , $1.2 <  \eta  \leq 2.1$ ) . . . . .	72
3.27	Efficiency with Absolute Isolation ( $p_T^{GMT}$ , $1.2 <  \eta  \leq 2.1$ ) . . . . .	73
3.28	Efficiency with Absolute Isolation ( $p_T^{SA}$ , $1.2 <  \eta  \leq 2.1$ ) . . . . .	73
4.1	Neutron Energy and Fluence in ME1/1 . . . . .	78
4.2	MPC Mezzanine Board . . . . .	83
4.3	Block Diagram of Spartan-6 FPGA Testing Setup . . . . .	84

# Tables

3.1	Detailed HCAL Tower Segmentation . . . . .	39
4.1	HL-LHC Neutron Exposure in ME1/1 . . . . .	79

## List of Acronyms and Initialisms

<b>AFEB</b>	Anode Front End Board
<b>ALCT</b>	Anode Local Charge Track
<b>BSM</b>	Beyond the Standard Model
<b>BX</b>	Bunch Crossing
<b>CCB</b>	Clock and Control Board
<b>CERN</b>	European Organization for Nuclear Research
<b>CFEB</b>	Cathode Front End Board
<b>CLB</b>	Configurable Logic Blocks
<b>CLCT</b>	Cathode Local Charge Track
<b>CMS</b>	Compact Muon Solenoid
<b>COTS</b>	Commercial Off-The-Shelf
<b>CSC</b>	Cathode Strip Chamber
<b>CSCTF</b>	Cathode Strip Chamber Track Finder
<b>DCFEB</b>	Digital Front End Board
<b>DT</b>	Drift Tube
<b>EB</b>	Electromagnetic Barrel

<b>ECAL</b>	Electromagnetic Calorimeter
<b>EE</b>	Electromagnetic Endcap
<b>FF</b>	Flip-Flops
<b>FPGA</b>	Field-Programmable Gate Array
<b>GMT</b>	Global Muon Trigger
<b>GT</b>	Global Trigger
<b>HB</b>	Hadronic Barrel
<b>HCAL</b>	Hadronic Calorimeter
<b>HE</b>	Hadronic Endcap
<b>HF</b>	Hadronic Forward
<b>HO</b>	Hadronic Outer
<b>HL-LHC</b>	High-Luminosity LHC
<b>L1</b>	Level-1 Trigger
<b>LCT</b>	Local Charged Track
<b>LHC</b>	Large Hadron Collider
<b>LS1</b>	Long Shutdown 1
<b>LS2</b>	Long Shutdown 2
<b>ME</b>	Muon Endcap
<b>MPC</b>	Muon Port Card
<b>MS</b>	Muon Sorter

<b>PMT</b>	Photomultiplier Tube
<b>PRBS</b>	Pseudo-Random Bit Stream
<b>QCD</b>	Quantum Chromodynamics
<b>RCT</b>	Regional Calorimeter Trigger
<b>ROC</b>	Rate of Change
<b>RPC</b>	Resistive Plate Chamber
<b>SEU</b>	Single Event Upset
<b>SM</b>	Standard Model
<b>SP</b>	Sector Processor
<b>TF</b>	Track Finder
<b>TMB</b>	Trigger Motherboard
<b>TMR</b>	Triple Module Redundancy
<b>VME</b>	Versa Module Europa
<b>WLS</b>	Wavelength Shifting

# Chapter 1

## Introduction and Motivation

### 1.1 Introduction to Particle Physics and the Standard Model

In the 1960's Glashow [1], Weinberg [2], and Salam [3] devised a theory, today known as electroweak theory, that unified the electromagnetic force with the weak force. This theory, along with the particles themselves, the theory of quantum chromodynamics (QCD), and related theories is known collectively as the Standard Model (SM). The Standard Model of particle physics is humanity's best effort to understand the physical world around us at the most fundamental level. This is no small undertaking, but the Standard Model of particle physics does it exceptionally well. The particles of the SM are shown in Figure 1.1.

The elementary particles of the Standard Model are categorized into three main groups: leptons, quarks, and intermediary gauge bosons. The quarks and leptons which make up all matter are fermions, while the particles that mediate their interactions are bosons. The leptons have spin, which is an intrinsic quantity and is, in units of angular momentum ( $\hbar = 6.582 \times 10^{-16}$  eV sec),  $\frac{1}{2}$ , and have an electromagnetic charge of  $\pm 1$  given in units of fractional electron charge ( $1 e = 1.602 \times 10^{-19}$

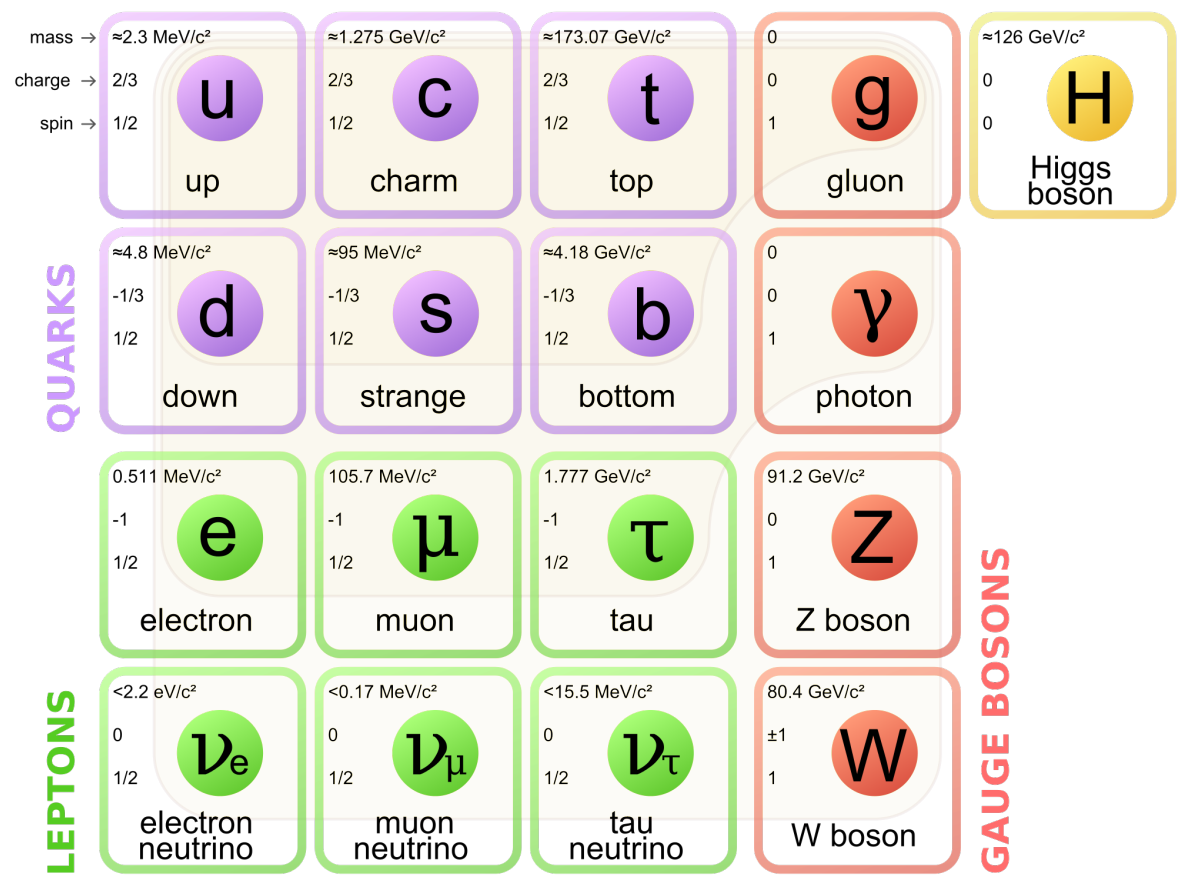


Figure 1.1 : The elementary particles of the Standard Model of particle physics. [4]

coulombs). There are three generations of leptons: the electron, muon, and tau generations, each accompanied by a zero charge, spin  $\frac{1}{2}$  neutrino. It is interesting to note that from an experimental point of view, neutrinos are nearly impossible to detect. Their existence is usually inferred from the missing energy in an event (which is itself inferred from the decay kinematics and calorimeter information). Similar to the leptons, the quarks also have three generations: the up and down; the charm and strange; and the top and bottom. The quarks have spin  $\frac{1}{2}$ , a fractional charge

of either  $-\frac{1}{3}$  or  $+\frac{2}{3}$ , and have the property of color<sup>i</sup>. Color is a conserved quantity and is analogous to the electromagnetic charge. Groups of quarks combine to form colorless, color singlet, states; these objects are called hadrons (such as the proton and neutron). The gauge bosons of the Standard Model all have spin 1, and mediate the interactions of the forces (strong, electromagnetic, and weak). The gluon mediates the strong force which applies to colored objects (the quarks). The photon mediates the electromagnetic interaction which takes place between all electrically charged objects. Finally, the W and Z bosons mediate the weak interaction which is responsible for nuclear radiation and particle decays.

It is the Higgs mechanism that is responsible for the electroweak symmetry breaking which gives rise to the massive W and Z bosons as well as the Higgs boson [6]. In July 2012 the discovery of the Higgs boson was announced by the Compact Muon Solenoid (CMS) and A Toroidal LHC Apparatus (ATLAS) experiments [7]. This discovery was another triumph of the Standard Model. The only force not included in the Standard Model is the gravitational force. Theories exist in which gravity is mediated by a so-called graviton; however, there is currently no experimental evidence for the existence of the graviton.

---

<sup>i</sup>“Color” is a misnomer and does not refer to a visual property of the particle, but instead represents an SU(3) symmetry [5].

## 1.2 Motivation for Further Study

The Standard Model is an incomplete theory. The omissions of the Standard Model include gravity, dark matter, and dark energy. There are many theories that attempt to fill in the gaps of the Standard Model (supersymmetry, string theory, and extra dimensions are among the most notable), but none of them have been definitively proven with current experimental data.

Research in particle physics at the European Organization for Nuclear Research (CERN) Large Hadron Collider (LHC) includes studies of all of the previous discussed topics and an investigation in to the properties of the newly discovered Higgs boson. The Particle Physics Project Prioritization Panel (P5) has prioritized U.S. particle physics to focus on the characteristics of the Higgs boson, physics accompanying the neutrino mass, ascertaining the origin of dark matter, dark energy, and the unknown (new particles, interactions, and physics) [8]. As a side note, advances in experimental particle physics have a long history of benefiting society by creating new technologies, and this tradition continues [8] [9].

## 1.3 Physics Motivation of the LHC and CMS Upgrades

The LHC contributes to the study of particle physics by focusing on the energy frontier. That is, very energetic particles are collided in order to create heavy states. Most collisions that take place at the LHC are proton-proton collisions (and it is

these collisions that are of interest to this thesis); however, heavy ion (lead-lead), and lead-proton collisions also take place. At the LHC, collisions, or events, are detected using large experiments such as the CMS detector, which relies on the scintillation and ionization of material by charged particles. It should be noted that this means that neutral particles, since they do not cause ionization to take place (and as such, do not leave a direct reconstructable track), may only be deduced from the conservation of energy and momentum, event kinematics, and calorimeter information (see Section 2.2.3). During the first run at the LHC from 2010-2012 (Run1) the LHC ran with a center of mass energy<sup>ii</sup> ( $\sqrt{s}$ ) of 7 and then 8 TeV (with each proton beam carrying half of the energy). The higher the center of mass energy, the higher the average mass of the resulting states produced, thus, increasing the likelihood of discovering new physics. In order to increase the capabilities of the LHC, it entered an upgrade period known as Long Shutdown 1 (LS1) in 2013 and is expected to resume physics in  $\sim 2015$ .

Throughout LS1, upgrades to the LHC are taking place which intend to increase the center of mass energy and the luminosity by a factor of 2 (to 14 TeV and  $2 \times 10^{34} \text{cm}^{-2} \text{sec}^{-1}$  respectively), and increase the frequency of proton-proton bunch crossings (BX) to 25ns (from 50ns). In order to fully take advantage of the upgraded

---

<sup>ii</sup>Center of mass energy is usually denoted using the Mandelstam variable:  $\sqrt{s}$ . See reference [6] for further information on the Mandelstam variables.

LHC environment, the CMS detector also requires upgrades. The specific upgrade of interest to the studies contained in this thesis pertains to the Level-1 (L1) Trigger. The L1 trigger is the first level of information discrimination in which coarse muon and calorimeter information from an event are used to determine whether the event data should be kept or thrown out. The upgraded LHC environment is expected to increase the trigger rate by a factor of 6 compared to pre-LS1 conditions. Since the L1 trigger is only capable of operating at  $100,000 \frac{\text{events}}{\text{sec}}$  and there will be  $\sim 50$  particle collisions per bunch crossing after the upgrade, the vast majority of collisions must be eliminated [10]. In order for the L1 trigger to operate effectively, only events which result in heavy states should be kept. In order for this to happen, clever algorithms must be implemented in order to quickly ( $\sim 3\mu\text{s}$ ) distinguish whether or not an event contains interesting physics (as outlined by the P5) to be studied [11].

This thesis focuses on both the hardware and algorithms associated with the L1 Trigger upgrade for the CMS endcap muon system at the CERN LHC. Chapter 2 discusses the CMS detector itself and the upgrades taking place during LS1. Chapter 3 focuses on an L1 trigger algorithm that I developed in order to reduce the trigger rate while maintaining effectiveness for selecting events related to interesting physics. Chapter 4 presents an L1 hardware radiation study in which I ensured that the upgraded hardware would operate correctly in the upgraded LHC environment. Chapter 5 provides a discussion of the results and future work is proposed based on the studies in

Chapters 3 and 4.

## Chapter 2

### The CMS Detector and its Upgrade

The Compact Muon Solenoid (CMS) detector is a large general purpose detector immersed in a  $\sim 4\text{T}$  magnetic field that is designed to investigate electroweak symmetry breaking, unified physical theories, supersymmetry, extra dimensions, and other phenomena at the TeV energy scale, as well as properties of the recently discovered Higgs boson [12]. The detector is composed of two broad structures, tracking systems and calorimeters, which work together in order to reconstruct particle collisions. Figure 2.1 shows an exploded view of the CMS detector, including all major components. For a full description of the CMS detector see reference [12]. The information on the CMS upgrade is based on the *Technical Proposal for the Upgrade of the CMS Detector Through 2020* [11], and the detailed description of the detector is from the *CMS Physics Technical Design Report Volume I: Detector Performance and Software* [13].

The CMS detector uses a coordinate system such that the beam axis corresponds with the  $z$  direction, and  $\theta$  is the polar coordinate (with respect to the beam axis).  $\phi$  is used to denote the azimuthal coordinate (with respect to the LHC plane). The coordinate system origin is taken to be the collision point which should be at the center of the detector. The pseudo-rapidity,  $\eta = -\ln(\tan(\frac{\theta}{2}))$ , is often used because

# CMS Detector

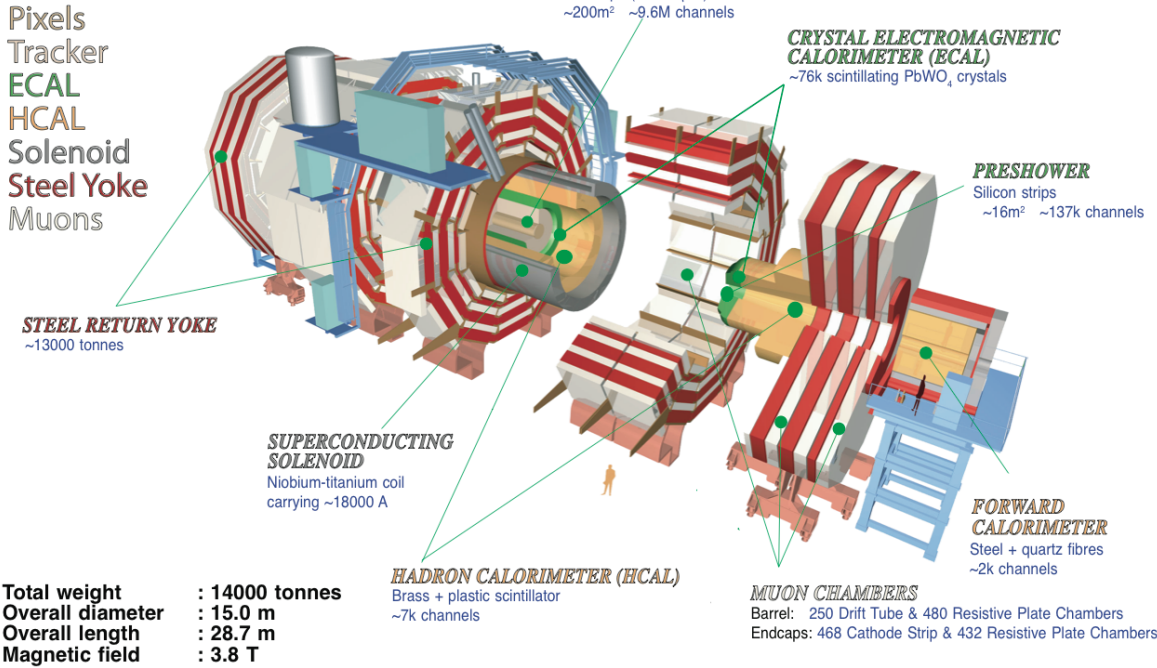


Figure 2.1 : Exploded view of the CMS detector showing all major components. [11]

particle collisions, or events, tend to be boosted in the z direction and  $\Delta\eta$  is a Lorentz invariant under boosts in the z direction. The transverse energy and momentum are also commonly used quantities and are defined as  $p_T = p \sin(\theta)$  and  $E_T = E \sin(\theta)$ , respectively [14].

## 2.1 Upgraded LHC Environment

From 2010-2012 the CERN LHC ran with an operational center of mass energy ( $\sqrt{s}$ ) of 7 and then 8 TeV, with a luminosity of  $\sim 10^{34} \text{cm}^{-2} \text{sec}^{-1}$ , corresponding to a total integrated luminosity of  $\sim 25 \text{fb}^{-1}$  of data [11]. Figure 2.2 shows the total integrated

luminosity from proton-proton collisions recorded by the CMS detector from the initial run (Run1). In 2013 the LHC entered a period known as Long Shutdown 1 (LS1). During LS1, the accelerator is not running so that repairs and upgrades may take place. These upgrades include improvements in order to increase the detector efficiency, to allow the CMS detector to function properly in a higher luminosity environment, and to fix known problems that were discovered during the initial running period.

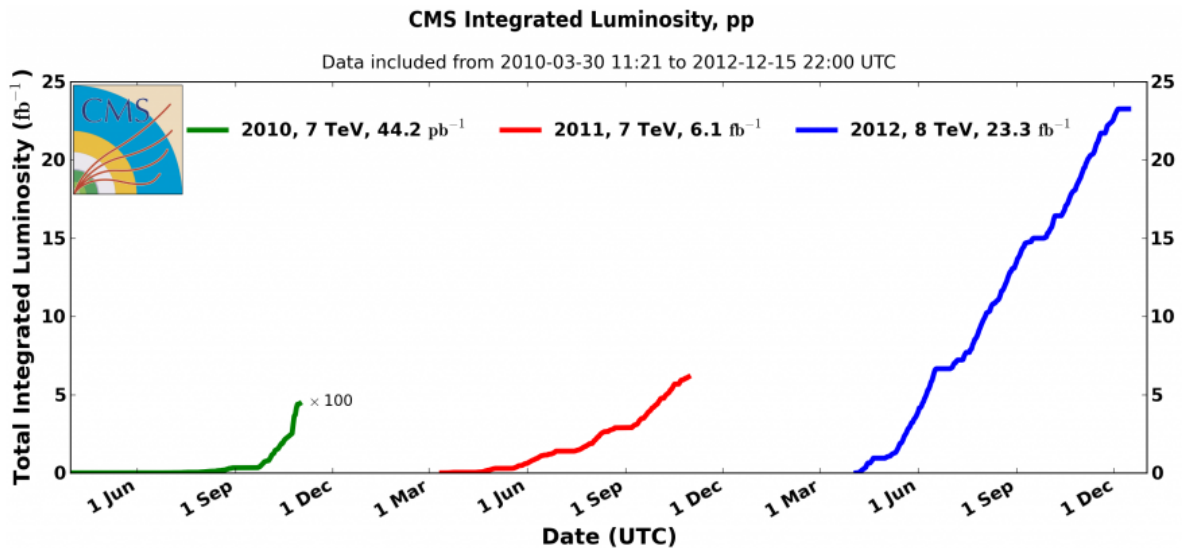


Figure 2.2 : The integrated luminosity taken by the CMS detector for proton-proton collisions during Run1. [15]

The primary goal of the LS1 upgrades are to ensure that the LHC and the CMS detector can run safely during operation with an energy and luminosity (14 TeV and  $\sim 2 \times 10^{34} \text{cm}^{-2} \text{sec}^{-1}$  respectively) exceeding the initial design values. In order for the

CMS detector to take full advantage of the increased LHC performance capabilities, upgrades to the detector must be completed in order to function at, and take advantage of, the higher energy and luminosity.

After LS1, the CMS detector is expected to take  $\sim 100 \text{ fb}^{-1}$  of data before shutting down for another set of upgrades in Long Shutdown 2 (LS2), and will effectively double the previously available search region in phase space and reachable mass scales [16]. The physics to be, tentatively, studied after LS2 will include the Higgs and related phenomena, electroweak physics, physics beyond the Standard Model (BSM), and improvements and confirmation of searches performed prior to LS1.

## 2.2 Upgrade of the CMS Detector

### 2.2.1 Tracking System

The tracking system is composed of two distinct silicon objects: the pixel detector and the microstrip detector. The pixel detector, seen in Figure 2.3, has three closely spaced layers and covers the barrel region ( $|\eta| \leq 0.8$ ) of the CMS detector, and includes two forward disks at each end. The pixel detector is primarily used for vertex finding. During a proton-proton bunch crossing (BX)  $\sim 20$  interactions take place. The overlap of these events at a particular crossing is known as “pileup.” It is the job of the pixel detector to be able to determine the initial points at which the protons interacted (primary vertices), and to which primary vertex each particle in the

event belongs. The microstrip detector has 10 layers that have a larger spacing than the pixel detector. The microstrip detector is used for track reconstruction and can measure the track bending radius and assign track  $p_T$ , where  $p_T$  is the momentum in the plane transverse to the proton beam axis. Section 2.2.2 details several of the important subtleties that are involved when fitting hits to a track and, consequently, determining the  $p_T$ . There are currently only plans to upgrade the pixel detector.

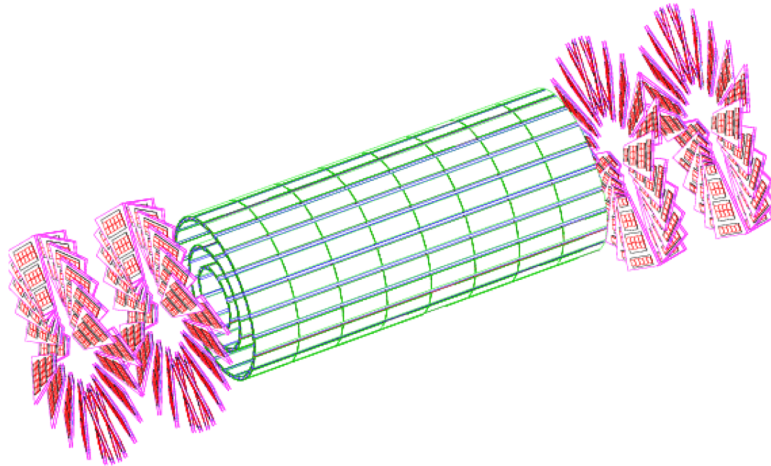


Figure 2.3 : The CMS pixel detector is made up of three concentric silicon pixel layers with two forward disks at each end. [13]

In 2016/2017, the pixel system will be upgraded to better accommodate the luminosity increase. This will be a major overhaul completely replacing the current 3-layer barrel 2-disk endcap system with a 4-layer barrel 3-disk endcap system. The upgraded pixel system is expected to provide the same level of accuracy seen during the initial run in the high luminosity environment.

### 2.2.2 Limits on Tracking Precision

Naïvely, track  $p_T$  may easily be determined since charged particles will follow a curved trajectory in a magnetic field. The hits found in the tracker are fit to a helix and then the cyclotron formula,

$$R = \frac{p_T c}{qB}, \quad (2.1)$$

is used to find the particle momentum. Here,  $p_T$  is the transverse momentum of the particle,  $c$  is the speed of light,  $q$  is the charge of the particle, and  $B$  is the strength of the magnetic field (which is in the z-direction at the CMS detector) [5]. The sign of the charge may be determined from the direction of curvature. However, there are several subtleties that must be included that limit tracking precision, and therefore,  $p_T$  assignment [17]. First, for each detector there is an inherent error in each hit measurement. For example, the Cathode Strip Chambers (discussed in detail in Section 2.2.4.1) provide a hit precision of  $\frac{1}{2}$  of a strip ( $\sim 8\text{mm}$ ) at L1. Next, the number of hits included in the fitting of a track add an error proportional to  $\frac{1}{\sqrt{N}}$  where  $N$  is the number of hits used in the fit (thus, more hits provide a more accurate fit). Also, there is an inherent error from the radius of curvature on the scale of  $\frac{1}{BL^2}$ , where  $B$  is the strength of the magnetic field and  $L$  is the lever arm (a larger lever arm and magnetic field lowers the error). Finally, multiple scattering (mostly due to Coulomb interactions) must be taken in to account. Multiple scattering interactions cause a particle to alter their path and lose energy as they pass through material (the

less material passed through, the less important the multiple scattering interactions are). The track precision error from multiple scattering interactions is proportional to  $\sqrt{\frac{l}{X}}$ , where  $l$  is the length of material passed through and  $X$  is the radiation length<sup>i</sup>. During final track reconstruction, all of these considerations are taken in to account.

## 2.2.3 Calorimeter System

### 2.2.3.1 The Electromagnetic Calorimeter

The electromagnetic calorimeter (ECAL) is used to measure the energy of particles that interact electromagnetically. Specifically, this means that the primary objective of the ECAL is to determine the energy of all charged particles and the photon. The ECAL is composed of lead tungstate crystals ( $\text{PbWO}_4$ ). Electromagnetic showers from bremsstrahlung radiation from the charged particles and pair production from high energy photons occurs in the crystals. The resulting lower energy particles then cause scintillation to occur inside of the ECAL. The photons from the scintillation are then detected and an energy of the incident particle can be determined. There are not upgrade plans for the ECAL during LS1.

---

<sup>i</sup>The radiation length is the distance that an electromagnetically interacting particle must travel in a medium before losing all but  $\frac{1}{e}$  of its energy. The radiation length is an especially important quantity because it determines the length scale for high energy electromagnetic cascades in a medium [18].

### 2.2.3.2 The Hadronic Calorimeter

The hadronic calorimeter (HCAL) is primarily used to measure the energy of hadrons, particles composed of quarks, and jets within  $|\eta| \leq 3$ . This is accomplished by using 18 depth layers of brass and scintillator. Hadronic interactions within the brass layers produce charged particles that then scintillate in the scintillator layers. The photons from the scintillation tiles are converted via wavelength shifting (WLS) fibers, and can be used to determine the particle energy.

The HCAL also includes an additional outer (HO), “tail-catcher,” so that showers are sampled over  $\sim 11$  interaction lengths<sup>ii</sup>. The forward region ( $|\eta|=3-5$ ) is assisted by a hadronic forward (HF) calorimeter made of iron and quartz fibers that produce Cherenkov light<sup>iii</sup> that can then be measured to determine the energy.

During LS1, the HCAL, barrel, endcap, and outer, (HB/HE/HO) will get improved photomultiplier tubes (PMTs) and photodetectors for more accurate energy determination. Additionally, new backend electronics will be created in order to send enhanced information to the regional calorimeter trigger (RCT). The hadronic for-

---

<sup>ii</sup>An interaction length is the average distance traveled by a particle in a medium before interacting and defined as  $l = \frac{1}{\sigma n}$ , where  $\sigma$  is the interaction cross-section and  $n$  is the number density of atoms in the medium.

<sup>iii</sup>Cherenkov light is radiation that is emitted by a charged particle that is in a medium such that the charged particle is moving faster than the speed of light in that medium.

ward (HF) will also receive upgraded PMTs.

### 2.2.4 The Muon System

The muon system, shown in Figure 2.4, is used to detect muons, and is composed of three subsystems located outside of the CMS solenoid and embedded in the return yoke of the magnet: cathode strip chambers (CSC), drift tubes (DT), and resistive plate chambers (RPC). The barrel region ( $|\eta| \leq 0.8$ ) contains the DTs ( $|\eta| \leq 1.2$ ) and RPCs ( $|\eta| \leq 2.1$ ), while the forward region ( $1.2 < |\eta| \leq 2.1$ ) contains the CSC ( $\sim 0.9 < |\eta| \leq 2.4$ ) and RPCs. In most cases ( $|\eta| \leq 2.1$ ) two of the muon subsystems send information to the Level-1 Trigger (see Section 2.2.5 for more information on the Level-1 Trigger). It is also possible in the overlap region,  $0.8 < |\eta| \leq 1.2$ , for a muon to pass through all three muon subsystems. Using the complete muon system information (from all three subsystems), the offline muon track reconstruction efficiency is 96-99% for muons with an offline  $p_T > 3\text{GeV}$  [11]. The number of muons produced that are to be detected in the forward (endcap) region is much higher than in the barrel region.

#### 2.2.4.1 Cathode Strip Chambers

The cathode strip chambers (CSC) are arranged in to 4 disks in each endcap. Each disk (or station) is composed of concentric rings of CSC chambers. Stations 2, 3, and 4 each have two rings of chambers with the inner ring containing 18 chambers and the outer ring containing 36 chambers. Note that station 4 has received its second ring of chambers as an upgrade during LS1. Station 1 is composed of three rings,

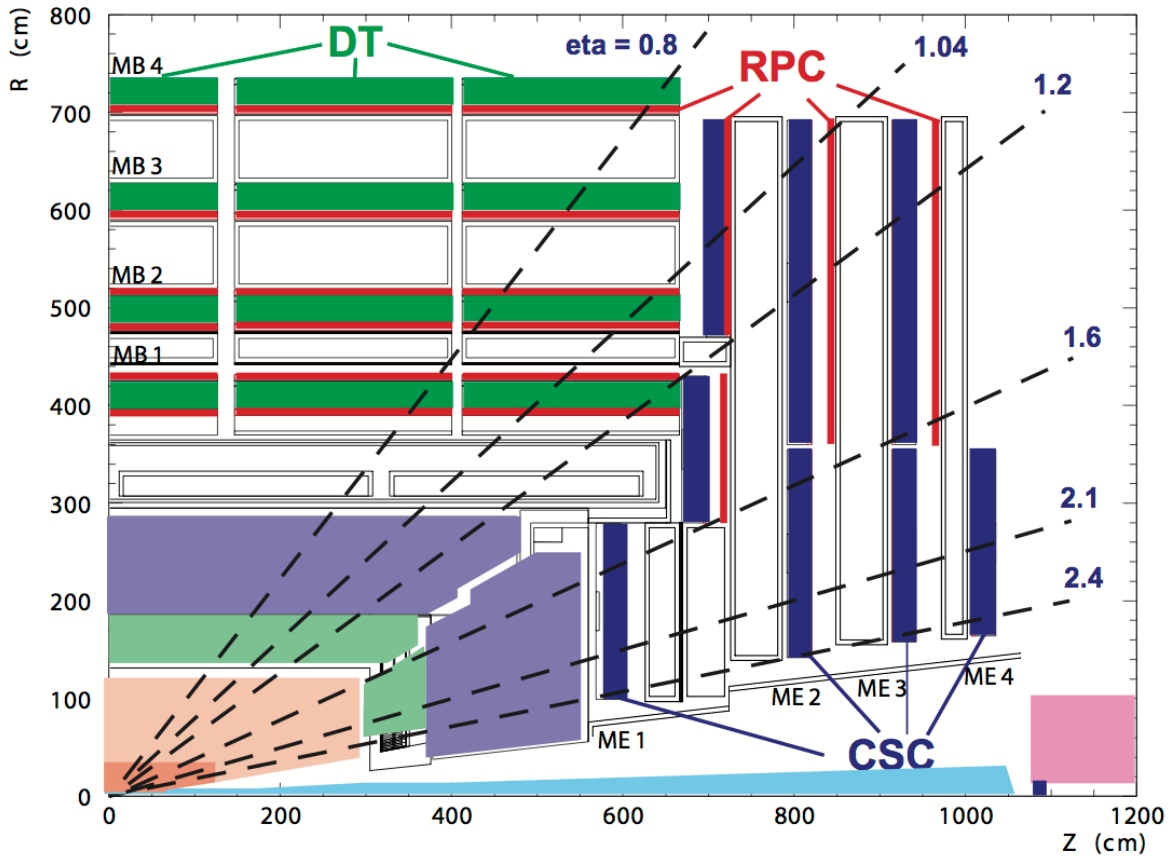


Figure 2.4 : The CMS Muon system is shown in r-z space including the drift tubes (DT), resistive plate chambers (RPC), and the cathode strip chambers (CSC). [13]

each with 36 chambers. When referencing the CSCs, it is the convention to label them as  $ME_{\pm}\langle\text{Station}\rangle/\langle\text{Ring}\rangle/\langle\text{Chamber}\rangle$  where ME stands for Muon Endcap, and the ring number counts outwards from the innermost ring [19]. The  $\pm$  is used to denote endcap and may be omitted when indicating generalities. Figure 2.5 shows the layout of the CSC disks and rings. It is important to note that ME1/1 is itself two layers, ME1/A and ME1/B, where ME1/A is the innermost of the two layers. The main difference between the two sections of ME1/1 is that ME1/A is not used for triggering purposes.

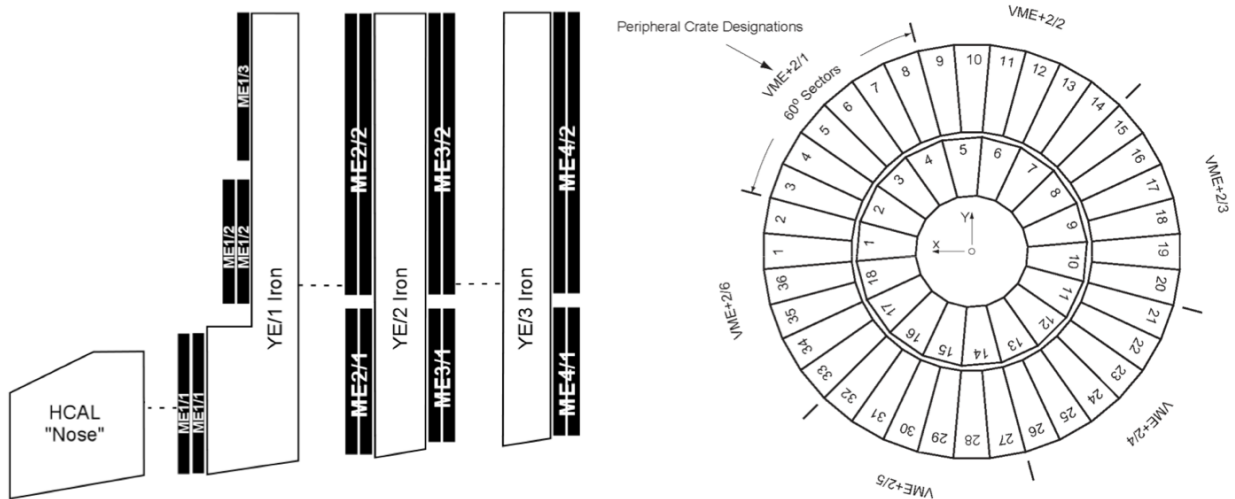


Figure 2.5 : Left shows the layout of the CSC rings in the x-z plane for a single quadrant of the CMS detector. Right shows the layout of the chambers for ME2/1 and ME2/2. This is the same layout for ME3 and ME4. ME1 is similar in essence, but has three rings and has 36 chambers per ring. [19]

Each CSC chamber is composed of six gaps, each containing a plane of radial cathode strips and perpendicular anode wires. Each layer of cathode strips are staggered by  $\frac{1}{2}$  of a strip ( $\sim 8\text{mm}$ ). When a charged particle passes through a CSC, the gas contained therein (a 30%-50%-20% mixture of Ar-CO<sub>2</sub>-CF<sub>4</sub> [20]) becomes ionized and produces an electron “avalanche.” Explicitly, this means that as the ejected electrons from the ionized gas travel towards the positively charged anode wires, since the electric field strength from the anode becomes stronger closer to it, the charged particles from the gas will increase in velocity. As the negative ions speed up, they will ionize more of the surrounding gas. The newly ionized particles continue this behavior and a so-called avalanche is created from the chain reaction. The resulting (nega-

tive) charge is then accumulated on the anode wires with a complimentary (positive) charge on the cathode strips. Figure 2.6 shows a schematic diagram of the process of a muon entering a cathode strip chamber, and the resultant induced charge produced.

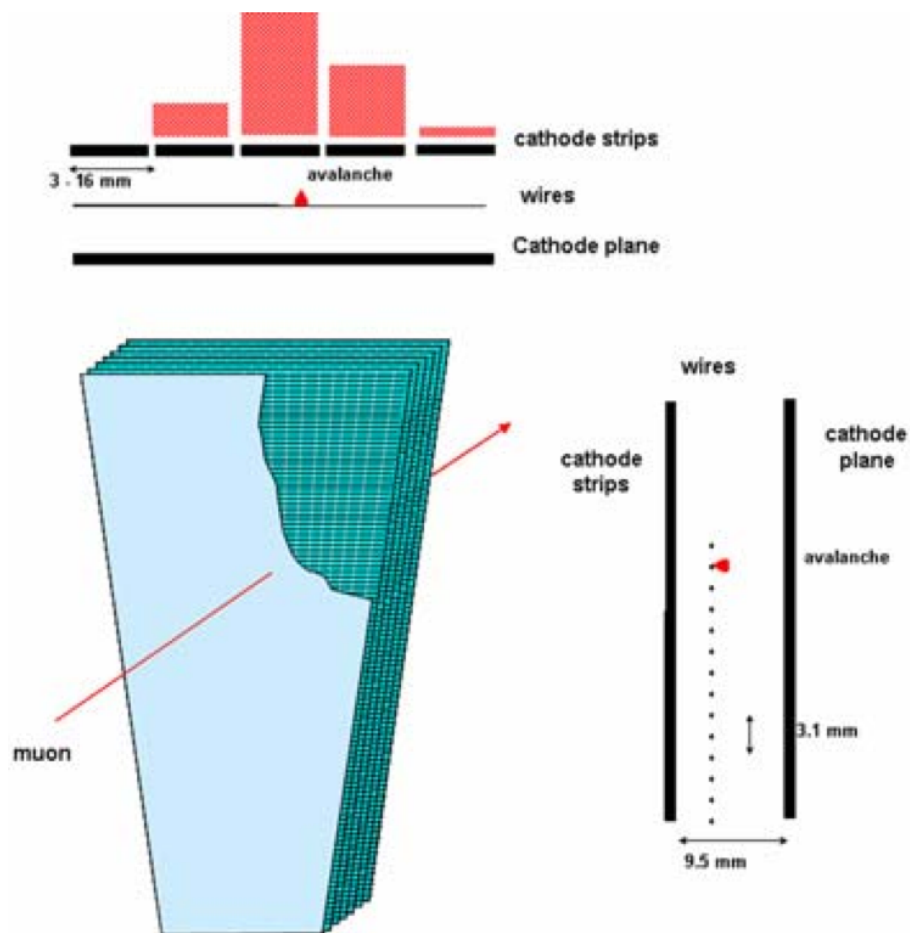


Figure 2.6 : A muon is shown entering the cathode strip chamber. An induced charge is produced and an electron avalanche is accumulated on the anode wires. The magnitude of the mirror charge on each cathode strip chambers is shown in peach. [21]

Ideally, each CSC chamber will record a charge measurement from a single incident

muon 6 times. Realistically, since the efficiency is not 100%, between 0-6 measurements are made. If at least two measurements are made then a “pretrigger” begins which allows for a delay of 1BX, and if there are at least 4 measurements then a trigger may be found [21]. In any case, this charge deposition from an incident muon will be distributed on multiple cathode strips. In order to send track information to the Level-1 Trigger (L1) quickly, the CSCs make use of a comparator. The comparator works by first finding all strips which have a local maximum of charge in each of the 6 layers of cathode strips. Once these charged strips are determined, the neighboring strip with the larger charge is identified. Once this is done for each layer, a probable muon path can be determined accurate to  $\frac{1}{2}$  of a strip [22]. Figure 2.7 shows the comparator process and track determination. Note that a more precise measurement of the hit position may be made by fitting the charge deposition to a Gaussian type distribution and then choosing a point of best fit to be the actual particle position. From this method, total spatial resolution of  $\sim 200\mu\text{m}$  with an angular resolution in  $\phi$  of  $\sim 10\text{mrad}$  may be determined. However, this higher level information is not available for use in the L1, and the L1 must make use of the  $\frac{1}{2}$  strip width resolution.

The following detailed information on the CSC follows the information given in references [23], [24], and [25]. The on-chamber mounted electronics include the Cathode Front End Boards (CFEB), Anode Front End Boards (AFEB), and Anode Local Charge Track (ALCT) card. The peripheral electronics are located within crates on

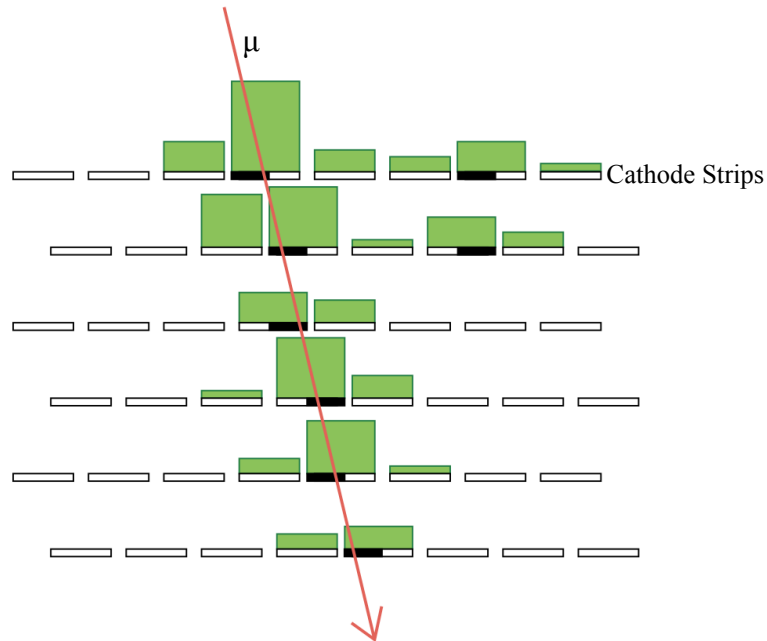


Figure 2.7 : An incident muon on a CSC chamber is shown passing through all 6 cathode strip layers. The magnitude of the resulting charge deposit is shown in green. Following the process of the comparator, the strip with larger charge neighboring the local maximums are identified. As shown in black, this allows the muon position to be determined accurate to  $\frac{1}{2}$  of a strip. [22]

the periphery of the return yokes and include the 9 Trigger Motherboards (TMB), and 1 Muon Port Card (MPC). The Track Finder (TF) crate is then located in the CMS Underground Support Cavern. Each TF crate includes 12 Sector Processors (SP), and 1 Muon Sorter (MS) board.

When a muon passes through a CSC chamber, the on chamber AFEB and CFEB amplify and digitize the signals from the anode wires and cathode strips respectively. The ALCT card then uses this information and creates the ALCT using the comparator step previously described. The output ALCT includes the anode pattern of hits

along with timing information and coarse radial position. The anode patterns (up to 2) are sent to the TMB from the ALCT card. The TMB then uses the cathode strip information to create a Cathode LCT (CLCT) complimentary to the ALCT. The ALCT and CLCT are combined at the TMB to create a single combined primitive known as an LCT. The LCTs contain information from the muon including the hit coordinates, the pattern type, and the trigger primitive quality. The TMB accomplishes this by using lookup tables rather than performing calculations. Lookup tables speed computation time by using arrays which store the input-output information from a process. Thus, rather than perform a calculation, an input is identified in a table and the corresponding output is found. ALCTs and CLCTs are found with a very high efficiency of 98.2% and 99.8% respectively [21]. The TMB then sends up to two LCTs to the MPC. The 3 best primitives (LCTs) are selected by the MPC and sent to the SP in the CSC Track Finder (CSCTF) crate. Aided by more lookup tables, the SP is then able to reconstruct up to 3 tracks. The SP then sends these tracks to the MS. The MS then selects the 4 best trigger tracks and transmits them to the Global Muon Trigger (GMT) where they are combined with the DT and RPC candidates. Figure 2.8 shows the flow of data from the CSC to the GMT. There are 60 peripheral crates and one CSCTF crate.

During LS1 the CSC will gain an additional fourth ring of chambers, ME 4/2, which will help to preserve a low  $p_T$  trigger threshold (more details on trigger thresholds

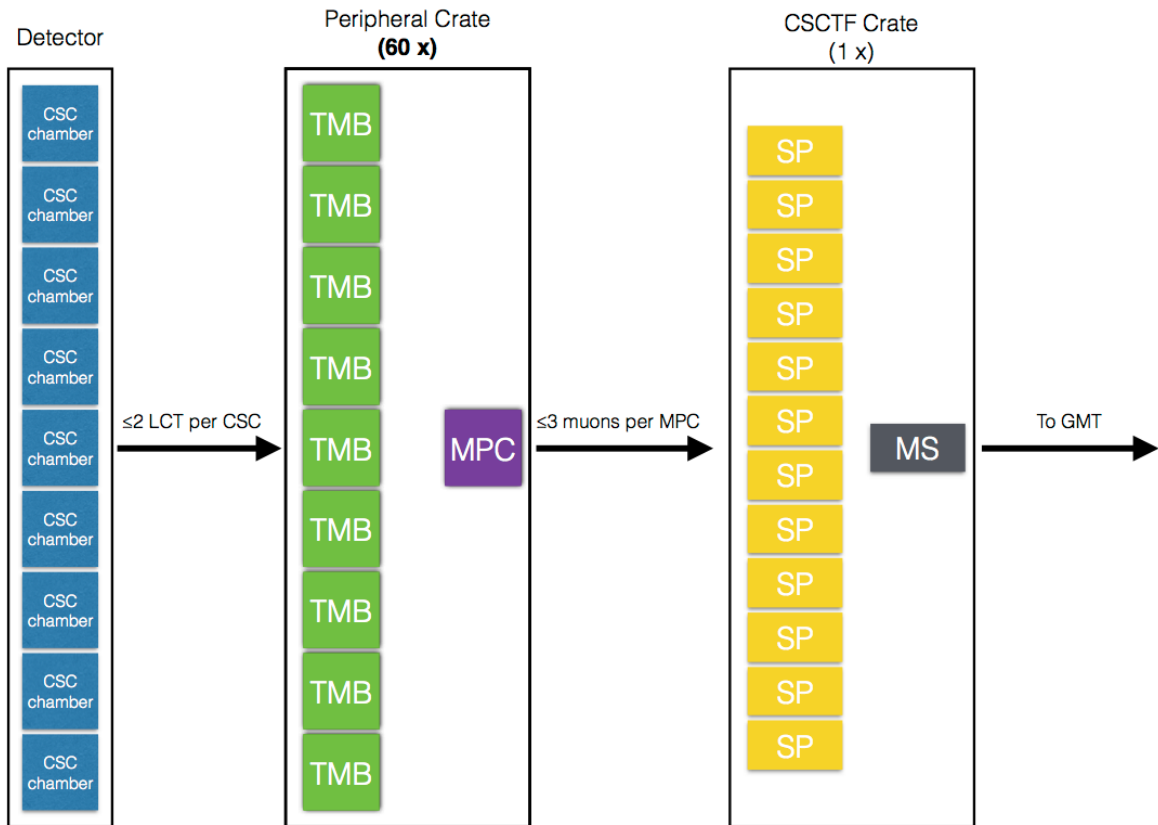


Figure 2.8 : The flow of data from the CSC to the GMT. [26]

can be found in Chapter 3). There will also be an upgrade of the ME1/A on chamber electronics. A detailed diagram of the ME1 CSC chamber (showing ME1/A) is shown in Figure 2.9. The current ME1/A chamber CFEB groups every 16<sup>th</sup> cathode strip together (and there are a total of 48 strips across each chamber layer) such that 3 strips are “triple-ganged” and read out together [11]. This means that there is an inherent ambiguity of muon hit placement in ME1 which can only be resolved by combining the ME1 information with that of the outer muon stations. The ME1/A station will be upgraded with new CSC “digital” front end boards (DCFEB) so that every cath-

ode strip may be read out separately, as opposed to the current triple-ganged method.

The new trigger primitive electronics will also deliver additional track segments to the upgraded CSCTF. Additionally, during the upgrade, the MPC mezzanine will be replaced and the CSCTF crate will be upgraded (specifically the SP). The MPC mezzanine upgrade will allow up to 18 LCTs per MPC to be sent to the SPs every bunch crossing (as opposed to the current limit of 3 LCTs per MPC). The CSCTF crate upgrades will allow for more bandwidth and more memory to accommodate the increased number of LCTs. These upgrades will also allow for more and better lookup tables for use in track finding. The lookup tables are created from simulated data and used for muon  $p_T$  assignment. Thus, the more robust the lookup table, the more accurate the muon  $p_T$  assignment. For a detailed description of the CSCTF upgrades see reference [27].

The upgraded MPC Mezzanine will require a new field-programmable gate array (FPGA). Chapter 4 details the radiation testing of one such upgrade FPGA candidate to ensure that it is capable of surviving the muon system radiation environment.

#### **2.2.4.2 Drift Tubes**

Each drift tube has a positively charged wire running through it and is filled with gas (a 85%-15% mixture of Ar-CO<sub>2</sub>) [29]. When a muon travels through the DT, the

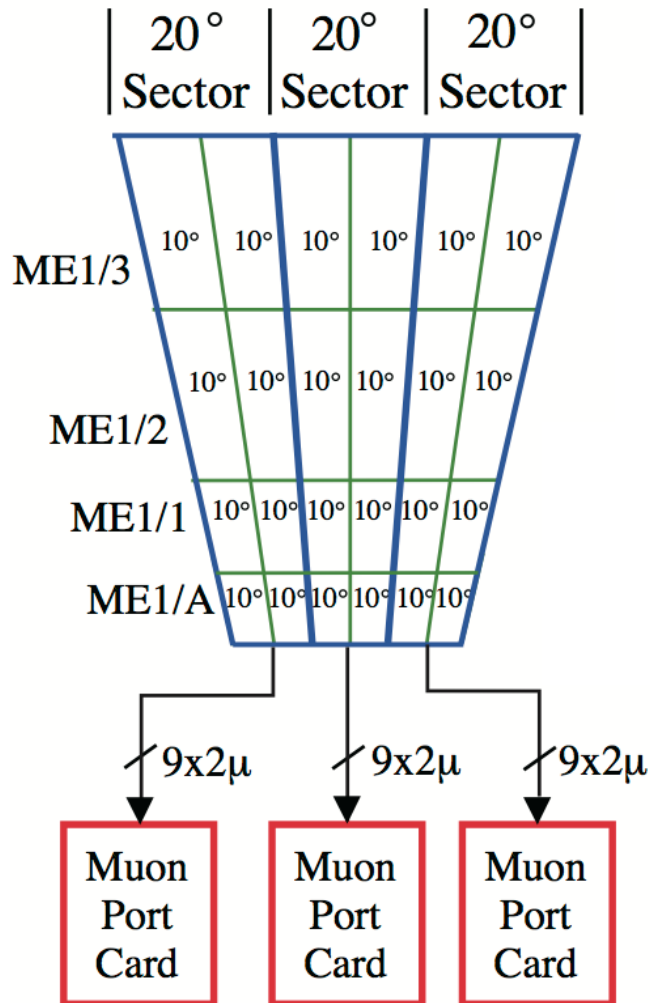


Figure 2.9 : A detailed schematic diagram of an ME1 CSC chamber. Each of the 9 TMBs send up to 2 muon candidates (LCTs) to the MPC. [28]

gas becomes ionized and electrons move to the wire. From the timing and position of the electrons when they hit the wire a spatial position of the muon can be determined. Each DT is staggered in order to give a spatial resolution of  $\sim 100\mu\text{m}$  and a  $\phi$  resolution of  $\sim 1\text{mrad}$ . There are 250 such chambers composing 4 layers. Figure 2.10 shows an incident muon on a drift tube chamber.

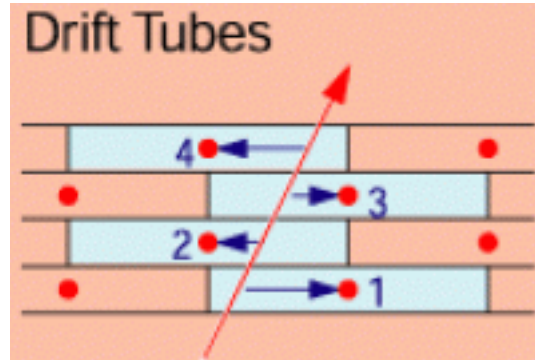


Figure 2.10 : A muon is shown entering the drift tube chamber. Electrons from the ionized gas move towards the wire (shown in red going in to the page). This information is sent to the L1 Trigger. [30]

No major upgrades are being supplied to the drift tubes during LS1; however, maintenance is being conducted.

### 2.2.4.3 Resistive Plate Chambers

The resistive plate chambers (RPCs) are composed of two parallel resistive plates, one anode and one cathode, in a gas environment (a 95.2%-4.5%-0.3% mixture of  $C_2H_2F_4-C_4H_{10}-SF_6$ ) [31]. When a muon passes through the RPC the gas becomes ionized and an avalanche of electrons is created. The charge deposition from the electrons is recorded by the detecting strips. Based on the charge deposition pattern the timing and position of the muon can be determined. The RPC provides extremely accurate timing information of incident muons ( $\leq 3ns$ ) to the L1 trigger [31]. This

timing resolution is superior to both the CSC and the DT, and is used to help determine from which primary vertex a muon originated. However, the spatial resolution provided by the RPC is not as precise as that of the CSC or DT. Figure 2.11 shows a schematic diagram of a resistive plate chamber.

In addition to the CSC effort to preserve a low  $p_T$  trigger threshold, additional RPCs will be added to the endcap muon system during LS1. The additional fourth layer of RPCs will extend coverage to  $|\eta| = 1.6$ . Eventually, most likely during LS2, the RPC will be extended to cover to  $|\eta| < 2.1$ .

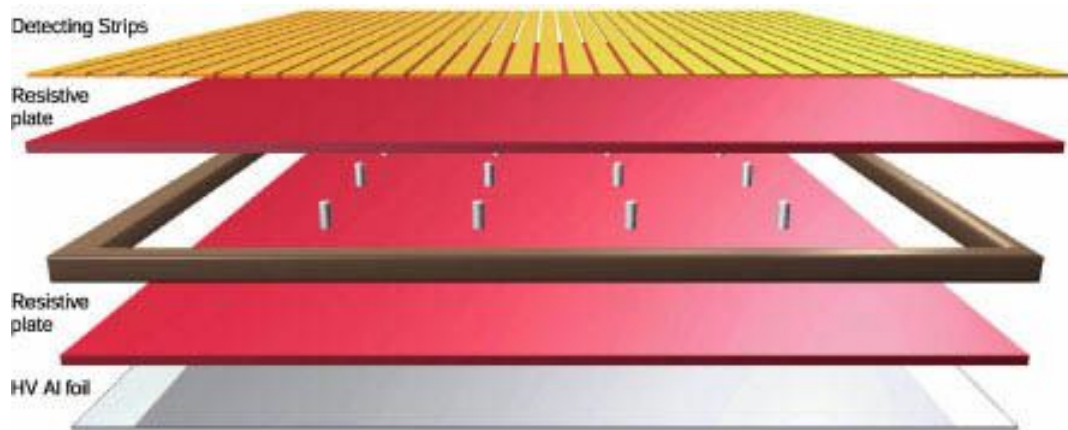


Figure 2.11 : A schematic diagram of an RPC. [32]

### 2.2.5 L1 Trigger Upgrade

Most collisions are “soft” collisions, meaning that there are no resulting high mass states. The Level-1 trigger is designed to eliminate these soft events and only keep

“hard” collisions (in which there could be high mass states). Since there is a beam crossing every 25ns the L1 trigger does not have time to use the complete data set, and instead, must use partial data from an event to decide whether or not it should be kept. The L1 must make a decision on whether or not an event should be kept in  $\sim 3\mu s$ , and can allow a maximum of  $100,000 \frac{events}{sec}$  to trigger [10]. During this time, the full event information is pipelined to accommodate for the delay caused by trigger processing [33]. After LS1 the pileup is expected to double resulting in a deterioration of the L1 event selection efficiency, specifically, the ability of the L1 to eliminate soft collision events and keep the hard collision events. In order to accommodate for the high luminosity environment and remain efficient, the L1 trigger requires upgrades to the hadronic calorimeter (HCAL) and the muon system.

In order to process additional information, the trigger system electronics outside of the CMS cavern will change from the current versa module europa (VME) system to  $\mu$ -TCA interconnections. The main difference between the connections is that in the VME system the information was bussed<sup>iv</sup>, while in the  $\mu$ -TCA system it is point-to-point. This makes the  $\mu$ -TCA system much faster during operation since not all information is sent to all components (rather, components only receive the information that they need), and will increase the bandwidth and speed with which the

---

<sup>iv</sup>A bus is a connection in which all information flows through and is used to reduce the number of physical pathways needed in electronics.

electronics can operate. The Regional Calorimeter Trigger (RCT) will also be rebuilt with this new technology and, thus, be able to take advantage of the full data set from the calorimeter front end. This will allow for more advanced trigger algorithms in the L1, such as isolation (see Chapter 3), to be implemented as well as accommodate higher trigger rates. In addition to the upgrades discussed in Section 2.2.4.1, the CSC Track Finder firmware and software will also be upgraded in order to accommodate the upgraded muon system, including the new chamber, ME4/2, and the upgraded ME1/1 electronics, to use the new input track segments and increase performance. Further, the RPC track finder will also be altered in order to accommodate the new RPC plane. Also, the DT track finder will be adjusted in order to accommodate the new trigger technologies.

The Global Muon Trigger (GMT) will also be upgraded. Currently, the GMT is where the trigger primitives from the three muon subsystems are combined and redundant muons are eliminated (especially in the overlap region where a single muon may have been recorded by both the CSC and RPC in the endcap, and the RPC and DT in the barrel region). The upgraded GMT will allow for more sophisticated algorithms, including isolation and “ghost busting.” Ghost busting is a more advanced method of eliminating superfluous muons within a single track finder crate [34]. GMT muon isolation is described in detail in Chapter 3.

## Chapter 3

### GMT Muon Isolation

The upgraded CSC Muon Sorter (MS) in the CMS endcap allows for the possibility of new, more sophisticated, algorithms in the Level-1 (L1) Trigger. In conjunction with the increased data transfer capabilities provided by the  $\mu$ -TCA connections, the MS may also have new physical connections that would allow additional information to be incorporated in to the trigger calculations that was previously unavailable. Specifically, this would allow the MS to receive calorimeter data, or send the muon trigger tracks to the calorimeter system. In either case, the calorimeter and muon information would be available at the Global Muon Trigger (GMT). The GMT would then be able to use this information in conjunction to introduce a muon isolation trigger (so-called GMT muon isolation) at L1.

This study investigates the usefulness of GMT muon isolation in the upgraded L1 system as a tool for lowering the L1 muon trigger rate while keeping the muon  $p_T$  trigger threshold low and maintaining a high efficiency. In this chapter, the efficiency is taken to mean the ability of the L1 trigger to accept low  $p_T$  muons from heavy decay states and reject those from hadronic behavior. This is explained in detail in Section 3.6.1.

### 3.1 Physics After LS1

The L1 Trigger was designed to operate with a rate of up to  $100,000 \frac{events}{sec}$ . After LS1, the luminosity is expected to increase by a factor of 2 (to  $2 \times 10^{34} cm^{-2} sec^{-1}$ ), the center of mass energy will increase from 8TeV to  $\sim 14$ TeV, and the pile-up will increase by a factor of 2 (to  $\sim 50 \frac{events}{BX}$ ). If changes are not made to the Level-1 trigger hardware, the L1 trigger rate is expected to increase by 6 [24].

The L1 trigger rate and trigger  $p_T$  threshold is closely related. The L1 trigger rate is measured in units of events, or triggers, per second. An event is triggered upon if specific criteria are met. An event that has triggered contributes to the trigger rate. This study focuses on the single muon  $p_T$  trigger, which “triggers” on the muon  $p_T$ . Explicitly, if an event contains a muon with a  $p_T$  greater than or equal to the trigger  $p_T$  threshold, then the event contributes to the rate. Therefore, as the trigger  $p_T$  threshold is lowered, the L1 trigger rate will increase.

Since the current hardware cannot handle a rate increase of a factor of 6, increased  $p_T$  trigger thresholds may be implemented in order to lower the rate. Muon trigger  $p_T$  thresholds eliminate triggering on most muons from jets and are an easy way to control the rate. However, there is a limit to how well a large trigger  $p_T$  threshold can work, especially in the endcap where track bending resolution (and therefore track  $p_T$  resolution) is low. Track bending resolution is low in the endcap, mainly, because

of the amount of material that a muon must pass through in the muon system. This leads to multiple scattering interactions and energy loss (see Section 2.2.2 for details).

Further, a high muon  $p_T$  trigger threshold would mean that lower  $p_T$  muons (with a  $p_T \leq \text{threshold } p_T$ ) would be lost and may have been decay products of interesting or high energy processes. A low  $p_T$  muon resulting as a decay product from a heavy state is especially likely in the endcap. For example, if a heavy state has high momentum in the direction of the beam-axis and decays to, say, two muons (forward and backward, one in to each endcap), the backwards muon will have very low  $p_T$ . Clearly, it is desirable to keep low  $p_T$  muons that are products of heavy state decays, and eliminate low  $p_T$  muons from hadronic behavior (which are associated with jets). Implementing a  $p_T$  threshold large enough to control the rate on its own would mean losing sensitivity to the electroweak scale (to study Higgs coupling, and other phenomena) and TeV scale searches (to improve and confirm studies prior to LS1). The goal of this study is to investigate the use of GMT muon isolation for lowering the rate while maintaining a high efficiency for selecting muons related to interesting physics, especially in the endcap region.

### 3.2 Muon Production and Isolation

Figure 3.1 shows the dimuon invariant mass spectrum from the CMS 2010 data ( $\sqrt{s}=7$  TeV) corresponding to an integrated luminosity of  $40 \text{ pb}^{-1}$ , and the simulated Run1

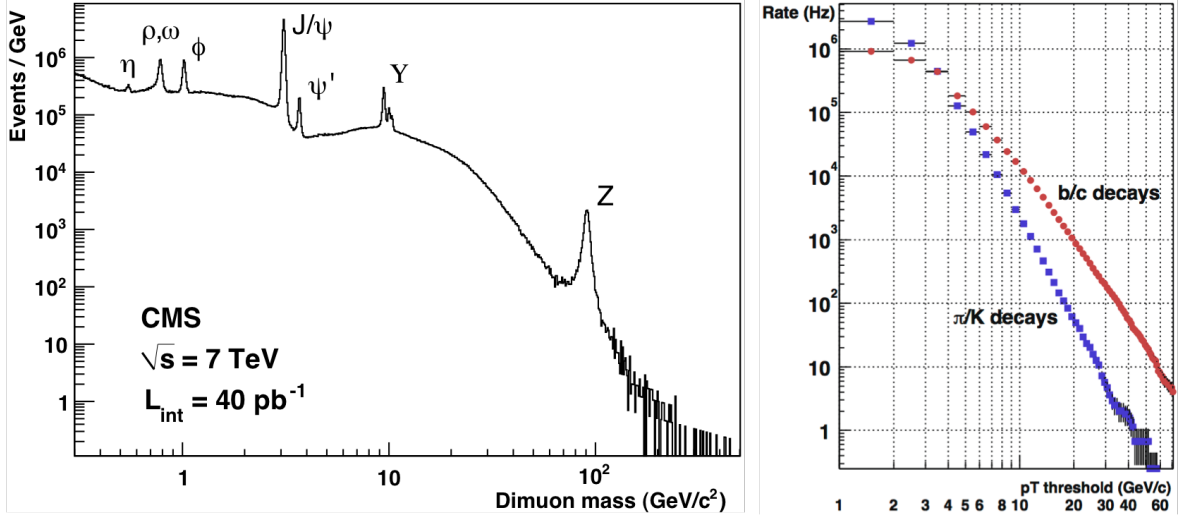


Figure 3.1 : Left shows the dimuon invariant mass spectrum from from the CMS 2010 data ( $\sqrt{s}=7$  TeV) corresponding to an integrated luminosity of  $40 \text{ pb}^{-1}$  [35]. Right shows the simulated Run1 rate ( $\frac{\text{muons}}{\text{sec}}$ ) of muons reaching the muon system from hadronic ( $\pi/K$  and  $b/c$ ) decays [28].

rate of muons reaching the muons system from hadronic ( $\pi/K$  and  $b/c$ ) decays. Muons in the trigger  $p_T$  threshold range ( $p_T \approx 10\text{-}30$  GeV) are most likely produced from  $b$  and  $c$  decays, and to a lesser extent from  $K$  and  $\pi$  decays [28]. These low  $p_T$  muons are usually from hadronic activity and are accompanied by wide jets, and should therefore, not be isolated in the calorimeter system. Muons with a  $p_T > \sim 30$  GeV are most likely decay products of heavy states. These muons are most likely to be isolated in the calorimeter system and only accompanied by pile-up and uncorrelated particles, since they are not associated with hadronic activity. Because of this dichotomy in muon behavior based on origin, muon isolation could be used to remove non-isolated, low  $p_T$ , muons associated with hadronic activity. Muon isolation may be calculated as either a relative or absolute quantity about the incident muon energy deposit:

$$Absolute\ Isolation = \sum_{region} E_T \quad (3.1)$$

$$Relative\ Isolation = \frac{\sum_{region} E_T}{p_{T,\mu}}. \quad (3.2)$$

Muon isolation used in conjunction with a  $p_T$  trigger threshold could act as an effective filter to control the rate. As an added benefit, this method would keep muons from lower energy decays such as the  $J/\psi$  and the  $\Upsilon$  that would otherwise be lost if the trigger  $p_T$  threshold were raised without requiring isolation.

The upgraded ( $\sim 2016$ ) L1 Trigger system allows for isolation to be calculated via two distinct methods. Either the calorimeter data can be sent to the Global Muon Trigger (GMT) (where isolation would then be calculated at the GMT), or the upgraded Muon Sorter can send the muon endcap information ( $|\eta| > 1.2$ ) to the calorimeter trigger. Sending the calorimeter information to the GMT would allow for 4x4 calorimeter tower, regional calorimeter trigger (RCT), isolation regions to be used (see Figure 3.2 right). Sending the Muon Sorter data to the calorimeter trigger would allow for full granularity, or 1x1, isolation regions to be used (see Figure 3.2 left).

There are currently no muon isolation requirements in the L1 system, and the calorimeter and muon trigger information are only combined at the Global Trigger (GT). Without utilizing the upgraded hardware, a jet-based isolation may be implemented

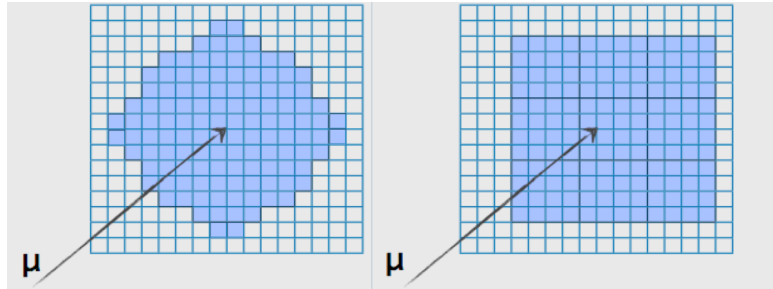


Figure 3.2 : Left shows a full granularity isolation region about a muon. Right shows a 3x3 RCT region isolation region about a muon. Each square on the grid represents a calorimeter tower.

wherein an event would be vetoed if a muon overlapped with a reconstructed jet. However, studies have shown that a jet-based isolation is not able to sufficiently reduce the rate [24].

This study considers both isolation region options (full granularity regions and RCT regions) for use in muon isolation in the L1 trigger, and tests their effectiveness for reducing the L1 trigger rate while maintaining a low trigger  $p_T$  threshold and high efficiency for selecting muons resulting from heavy decay states.

### 3.3 Data

To investigate the effectiveness of muon isolation in the L1 trigger, a study was performed using data that had been previously acquired by the CMS experiment. The entire 2012C data set from the CMS experiment at the LHC is used. For the

efficiency calculation (see Section 3.6.1), a  $Z(\mu\mu)$  sample<sup>i</sup> is used with a lumi-mask<sup>ii</sup>. The sample is skimmed such that only events that have an HLT isolated muon with a  $p_T \geq 24$  GeV, and are within  $|\eta| < 2.1$  (HLT\_IsoMu24). The events are also required to have a second muon with a  $p_T > 10$  GeV. The rate calculations (see Section 3.6.2) are performed with a SingleMu (minimum bias) sample from the 2012C data<sup>iii</sup> with the same lumi-mask as the  $Z(\mu\mu)$ . The minimum bias sample is a collection of events which are assembled using the loosest possible trigger requirements while ensuring that a soft collision has taken place (see reference [36] for further details). This minimum bias SingleMu sample has an open pass, meaning that no  $p_T$  restrictions are placed on the muons (HLT\_L1SingleMuOpen).

### 3.4 Emulation

The goal is to study muon isolation in the (GMT) L1 system. However, data does not yet exist for the upgraded system. Therefore, the trigger must be emulated. Emulation means that actual data will be manipulated in order to simulate the data that would have been received from the upgraded system. Specifically, the L1 trigger system and response with respect to the calorimeter data is being emulated. The upgraded L1 calorimeter towers are emulated with the SLHCUpgradeSimulations package [37]. Explicitly, actual data from the calorimeter towers are input in to the

---

<sup>i</sup>/SingleMu/Run2012C-Zmu-PromptSkim-v3/RAW-RECO

<sup>ii</sup>L1Trigger\_Run2012C\_JSON\_202500-204000\_v1.json

<sup>iii</sup>/Commissioning/Run2012C-PromptReco-v2/RECO

emulation package. The emulation package then alters the information to reflect the information that would have been received if the data had come from the upgraded offline system.

Since actual trigger data are being emulated (and there is no computer simulated data to check the veracity of the data at any step) it is important to verify that a reliable correlation between the actual information and the output of the emulation exists. Therefore, the emulated ECAL and HCAL data are independently appraised by comparing the actual Level-1 data with the emulated offline data. It is expected that the emulated data will accurately and dependably reflect the Level-1 data.

### **3.4.1 HCAL**

#### **3.4.1.1 Geometry and Segmentation**

The HCAL is portioned in to 2,088 calorimeter towers per quadrant that are denoted by  $i\eta$  and  $i\phi$  indices (see Figure 3.3). These calorimeter tower indices are defined such that the HCAL is uniform with the physical crystal sizes in the ECAL and are segmented according to Table 3.1. It should be noted that the  $\phi$  granularity increases from  $5^\circ$ - $10^\circ$  at  $i\eta=21$  ( $|\eta| = 1.740$ ). This is because the physical limit of the bending radius of the wavelength shifting (WLS) fiber readout must be accommodated. To force tower segmentation to be uniform with that of the ECAL, energies measured in towers with  $i\eta \geq 21$  are “artificially divided into equal shares and sent separately

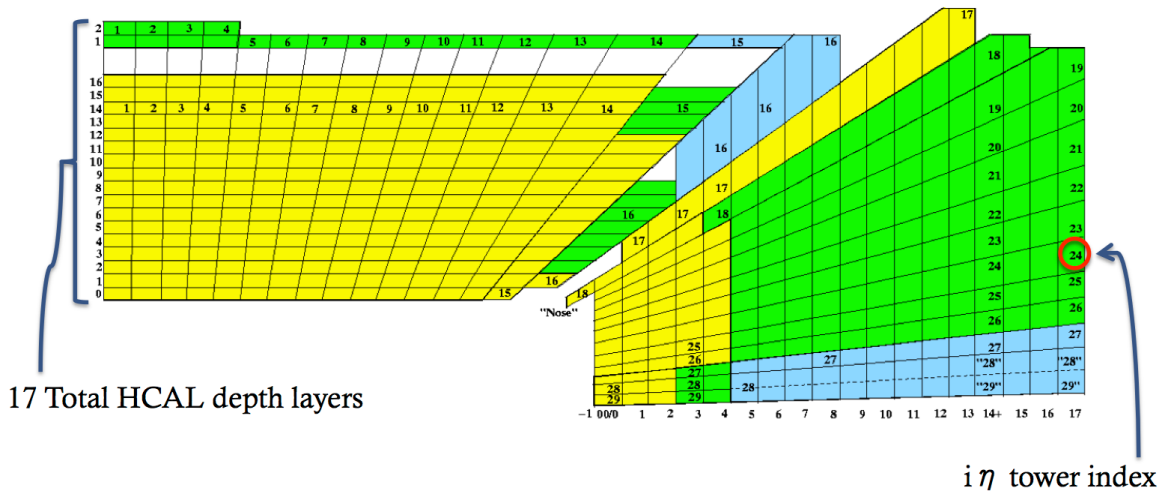


Figure 3.3 : HCAL tower mappings in r-z space for a single quadrant of the CMS detector. There are 72  $i_\phi$  towers (not shown) for each  $i_\eta$ . [24]

to the trigger” [13]. In doing so, the spatial resolution of the HCAL is artificially increased. This artificial segmentation is seen again in the first two depth segments (layer 0 and 1) of tower  $i_\eta=28$  and is shown in Figure 3.4.

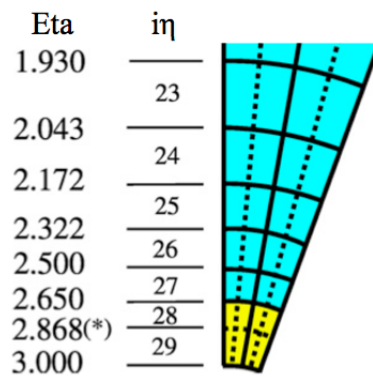


Figure 3.4 : Artificial tower segmentation is shown as a dashed line while physical segmentation is shown as a solid line. The yellow towers are in the forward region (HF), and the cyan is the endcap (HE) region. [13]

Tower index	$ \eta_{max} $	Detector	Size	
			$\eta$	$\phi$
1-15	$0.087 \times \eta$	HB	0.087	$5^\circ$
16	1.392	HB, HE	0.087	$5^\circ$
17-20	$0.087 \times \eta$	HE	0.087	$5^\circ$
21	1.830	HE	0.090	$5^\circ$
22	1.930	HE	0.100	$5^\circ$
23	2.043	HE	0.113	$5^\circ$
24	2.172	HE	0.129	$5^\circ$
25	2.322	HE	0.150	$5^\circ$
26	2.500	HE	0.178	$5^\circ$
27	2.650	HE	0.150	$5^\circ$
28	3.000	HE	0.350	$5^\circ$
29	3.314	HF	0.461	$20^\circ$
30	3.839	HF	0.525	$20^\circ$
31	4.363	HF	0.524	$20^\circ$
32	5.191	HF	0.828	$20^\circ$

Table 3.1 : HCAL tower segmentation in  $\eta$  and  $\phi$  is shown. The corresponding calorimeter regions are also specified: barrel (HB), endcap (HE), and forward (HF). [13]

### 3.4.1.2 Emulated $E_T$ vs HCAL Data Comparison

To verify the emulated information, the actual HCAL data and the emulated data must show good agreement (and it is determined that they do). Each trigger tower  $E_T$  (online, actual data) is compared to the corresponding emulated offline tower  $E_T$ . When matching the trigger towers to the offline towers all of the artificial segmentation and tower splitting must be taken in to account. For trigger towers with  $i\eta < 21$ , the matching criteria are simple: if the trigger towers and offline towers have the

same tower indices (both  $i_\eta$  and  $i_\phi$ ) then the  $E_T$  is compared directly. For trigger towers with  $21 \leq i_\eta < 28$  the offline tower energy is split, as described in the previous section, 3.4.1.1, since the emulated offline towers do not show  $E_T$  values for even-valued  $i_\phi$  (artificial) towers. To rectify this discrepancy, the offline tower energy is manipulated to preserve the accuracy of the actual, online, data. The same results could be achieved by adjusting the online calorimeter towers instead; however, in an effort to preserve the integrity of the actual data, the online calorimeter towers were left unaltered. Since this analysis is mainly concerned with the muon system which ends at  $|\eta| = 2.4$ , towers  $i_\eta \geq 28$  are ignored and will not contribute towards isolation region energy summations.

With these considerations accounted for, Figure 3.5 shows the comparison between the trigger tower and emulated offline tower HCAL  $E_T$ . For completeness, the unadjusted (naïve plot in which artificial tower segmentation is not accounted for)  $E_T$  comparison is also shown. It is clear that accommodations for the artificial towers must be made, as expected, and that a good correlation exists between the actual online data and the emulated offline data. The offline towers have categorically lower  $E_T$  than the emulated towers. However, this scale factor is unimportant, since all towers are equally influenced, and will not impact the effectiveness of isolation. As shown in Figure 3.6, the same behavior is seen over all calorimeter regions (defined by  $|\eta|$ ).

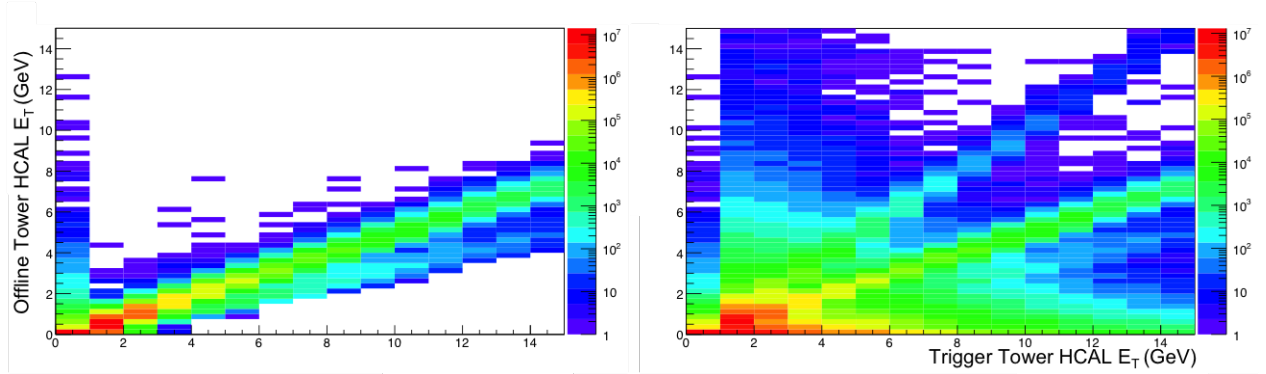


Figure 3.5 : The online/offline HCAL  $E_T$  comparison is shown. Left shows the comparison properly accounting for the artificial tower segmentation. Right is the unadjusted  $E_T$  comparison.

Since a linear correlation is apparent in Figure 3.6 and Figure 3.5, it may be concluded that a reliable correlation exists between the actual online data and the emulated offline HCAL data.

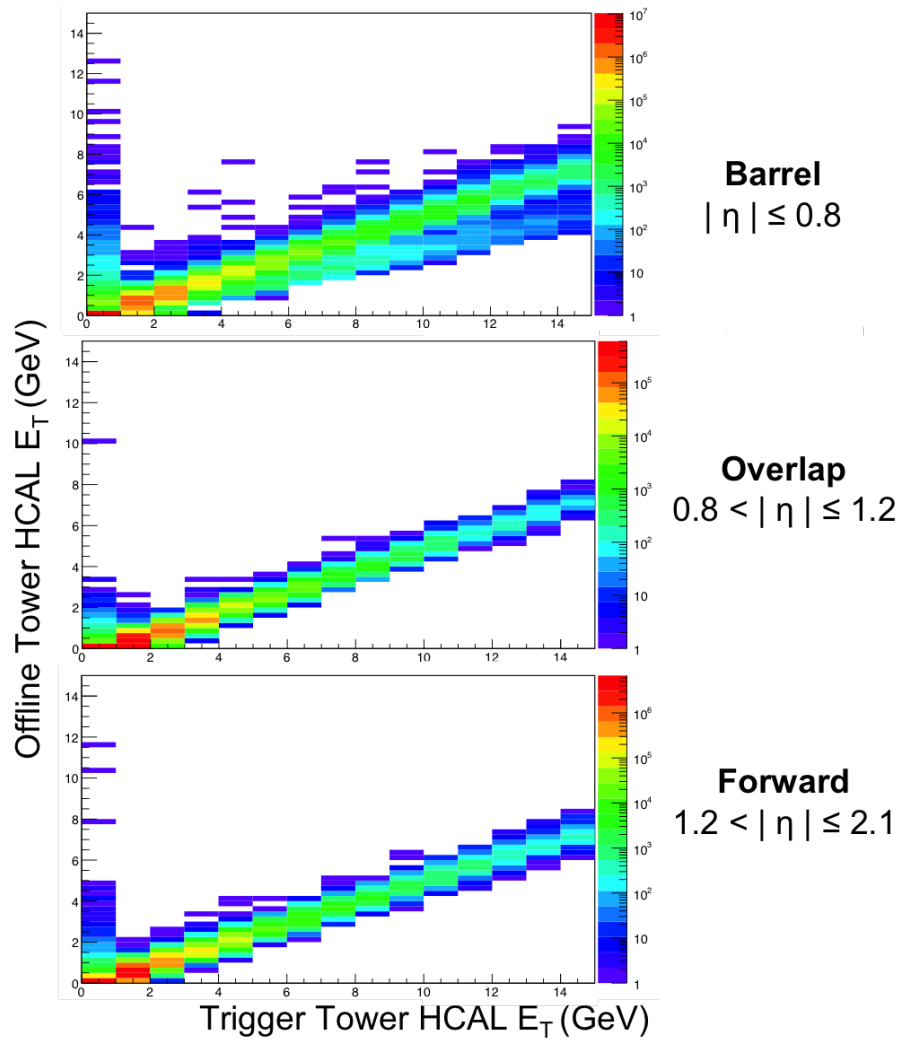


Figure 3.6 : This is the same emulated offline tower vs trigger tower  $E_T$  comparison plot as seen in Figure 3.5 (left), broken up by calorimeter region based on  $|\eta|$ . Artificial tower segmentation has been accounted for.

### 3.4.2 ECAL

#### 3.4.2.1 Emulated $E_T$ ECAL Data Comparison

As was done with the HCAL, the ECAL online calorimeter tower data must be compared to the emulated offline calorimeter tower data in order to verify the veracity of the emulation package. A schematic diagram of the ECAL tower mappings (including the HCAL) can be seen in Figure 3.7.

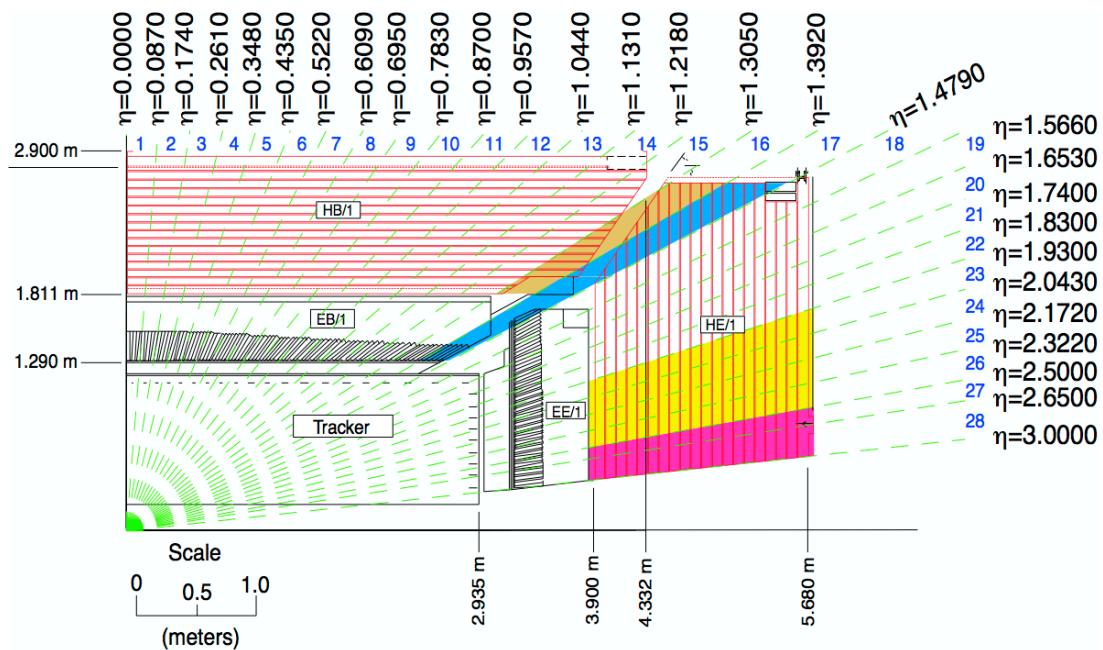


Figure 3.7 : ECAL tower mappings in  $r$ - $z$  space for a single quadrant of the CMS detector. Also shown is how the ECAL and HCAL fit together around the tracker. The naming convention is as the previous section: ECAL barrel (EB), HCAL barrel (HB), ECAL endcap (EE), HCAL endcap (HE). [38]

Compared to the HCAL, few adjustments need to be made to the emulated offline calorimeter towers since there is no artificial tower splitting. Further, the ECAL

does not physically increase in granularity at  $i\eta \geq 21$ . Despite this, it is found that although even-valued  $i\phi$  and  $i\eta \geq 21$  towers exist in the trigger (online) information as expected, the emulation package removes this information and combines neighboring tower data. This process effectively acts as an artificial resolution impairment since by using offline data only, there is no way to distinguish between an energy deposit in even-valued  $i\phi$  and  $i\phi - 1$  for  $i\eta \geq 21$ . Since these towers are physically distinct objects and could have recorded vastly different energies, there is no way to “re-split” the towers in a process similar to that undertaken for the HCAL towers. This causes a smearing effect that is seen when the trigger tower ECAL  $E_T$  is compared to the emulated offline ECAL  $E_T$  as seen in Figure 3.8. It is clear that the smearing effect is more prominent for lower energy tower deposits and does not change the general behavior of the comparison plot. Overall, there is a good correlation between the trigger tower ECAL  $E_T$  and the emulated offline tower ECAL  $E_T$ , and the same scaling effect is seen for the ECAL as was seen in Figure 3.5 for the HCAL.

Since both the ECAL and the HCAL show a reliable correlation between the online trigger tower  $E_T$  and the emulated offline  $E_T$  it may be concluded that the upgraded calorimeter towers are accurately emulated. Therefore, it is expected that the results from isolation in the following sections are accurate, and can be used to determine the realistic expectations of rate reduction (and efficiency loss) from the use of GMT muon isolation in the upgraded L1 system.

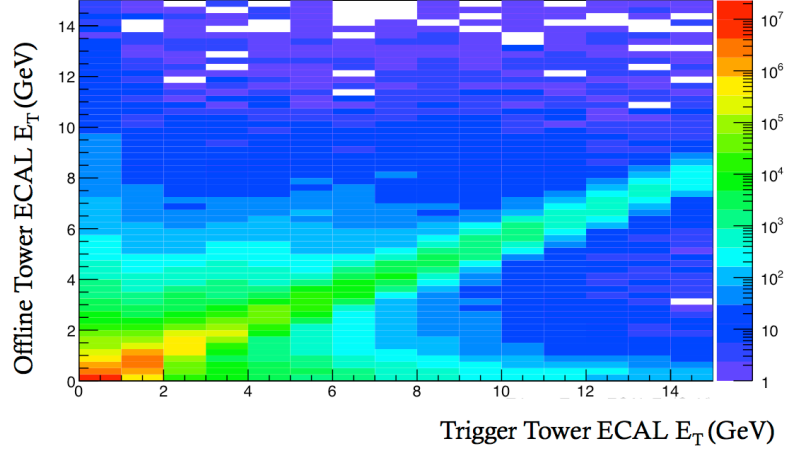


Figure 3.8 : The online/offline ECAL  $E_T$  is shown.

### 3.5 RCT Region Map

Rather than using an upgraded Muon Sorter to send muon data to the calorimeter trigger, the calorimeter data could be sent to the MS. However, the full granularity calorimeter data could not be used because of data transfer limitations so only calorimeter region data could be utilized. Specifically, in this scenario, only 4x4 calorimeter tower regions (RCT regions) would be available. RCT regions (see Figure 3.2), as used in GMT muon isolation, each cover an area of  $5.0 \times 0.7$  in  $\eta$ - $\phi$  space. RCT regions are mapped to  $i\eta$ - $i\phi$  space and assigned an identifying integer. This mapping is shown in Figure 3.9. In order to maintain a (roughly) constant physical area throughout the detector, the number of calorimeter towers that each region contains must change with  $\eta$ . RCT regions 0-20 are true 4x4 calorimeter tower regions covering  $\Delta\phi=0.348^\circ$ , regions 21-28 fall within the range of artificially split HCAL towers

( $21 \leq i\eta < 28$ ) and are 2x2 calorimeter tower regions (each tower covers  $\Delta\phi=0.174^\circ$ ). Finally, for RCT regions 29-32 each individual calorimeter tower covers  $\sim\Delta\phi=0.348^\circ$  so each tower is treated as an RCT region.

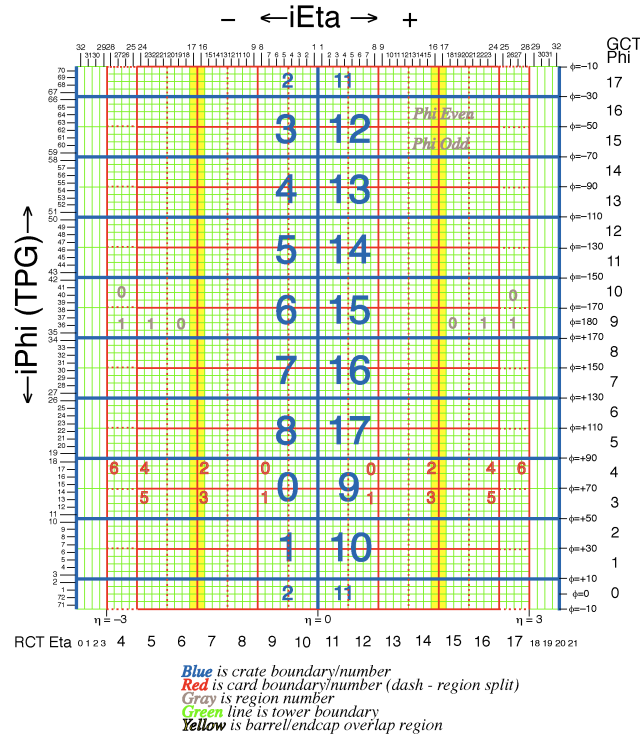


Figure 3.9 : RCT region map in  $i\eta$ - $i\phi$  space. [39]

As with the individual ECAL and HCAL tower  $E_T$ 's, Figure 3.10 shows a 3x3 RCT region  $E_T$  online/offline comparison. Although the 3x3 RCT regions seem to have a poor correlation between the online and offline information, using RCT regions for isolation has several potential advantages. The largest benefit is that RCT regions scale in size with  $\eta$  (in order to keep a constant physical size) since particle showers

keep a constant physical size regardless of position in  $\eta$ - $\phi$  space. In contrast, full granularity regions are a constant size in  $\eta$ - $\phi$  space. Although it is expected that full granularity regions should perform better than RCT regions under any isolation scenario because they are more precisely situated about the incident muon energy deposit in the calorimeter, they have a very small physical area in the high  $\eta$  region. Specifically, if the full granularity region radius is too small, which may be the case in the endcap, isolation would trivially be expected to lose effectiveness and perform poorly since the entire muon energy deposit in the calorimeter may not be included in the isolation region.

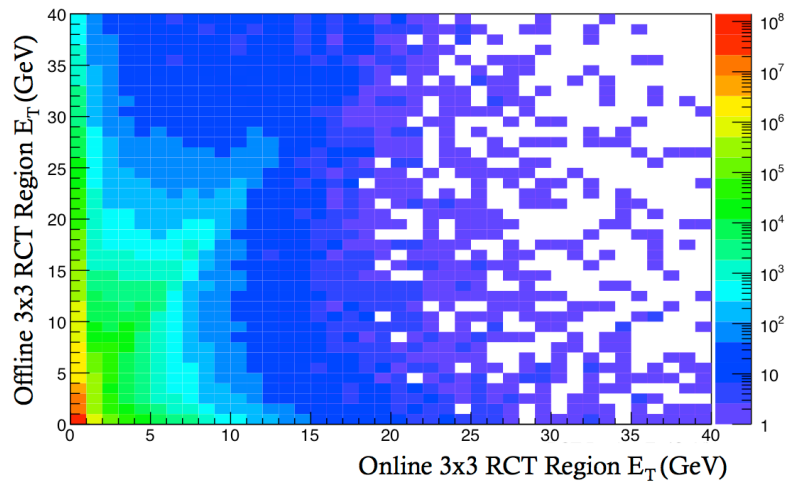


Figure 3.10 : The online/offline 3x3 RCT region  $E_T$  is shown. The region sum is equivalent to the absolute isolation (Equation 3.2).

## 3.6 Selection Criteria and Variable Definitions

The goal is to study the effectiveness of using GMT muon isolation in the upgraded L1 system in order to lower the single muon  $p_T$  threshold while maintaining a manageable trigger rate and a high efficiency for selecting isolated muons originating from non-hadronic behavior, principally in the endcap. So far, we have determined that the emulation data is valid. Next, the following evaluation quantities must be precisely defined mathematically: efficiency and relative efficiency; rate and relative rate; and absolute and relative isolation.

### 3.6.1 Relative Efficiency

The efficiency is determined via a counting “tag-and-probe” method. Where here, the efficiency refers to the ability of the L1 trigger to accept low  $p_T$  muons resulting from heavy decay states and reject those from hadronic behavior. Events are selected according to the offline data and must contain exactly two muons that:

1. share the same vertex;
2. are of opposite charge; and
3. have an invariant mass of  $91 \pm 15$  GeV<sup>iv</sup>.

Further, the event must also have exactly one “tag” and one “probe” muon. Of the two muons, the tag is selected as the muon to:

---

<sup>iv</sup>This value is  $\pm 15$  GeV of the Z boson mass.

1. have fired the HLT<sup>v</sup>;
2. have a  $p_T > 32$  GeV;
3. be within  $|\eta| < 2.1$ ;
4. meet the quality criteria for the tight muon selection<sup>vi</sup>; and
5. have a relative particle flow<sup>vii</sup> isolation  $< 0.1$  .

The remaining muon (not the tag) is then labeled as the probe if it:

1. has a  $p_T > 10$  GeV;
2. is within  $|\eta| < 2.1$ ; and
3. satisfies the criteria for a tight muon.

It is important to note that if both muons qualify as a tag, then they are both counted as a probe since there is no way to know which one fired the HLT, and the event is discarded.

---

<sup>v</sup>It must have an L1 candidate.

<sup>vi</sup>A tight muon is a muon candidate that is a global muon and also meets supplementary requirements to ensure that it is a strict quality candidate. Additional information on global muons and tight muons may be found in references [40] and [41] respectively.

<sup>vii</sup>Particle flow is a particle track reconstruction algorithm that uses hit and calorimeter information. By combining information, the particle flow algorithm can ensure that particle tracks lead to energy deposits in the calorimeter [42].

To find the efficiency, a GMT (online) candidate must match the (offline) probe. A match is found if there is a GMT candidate which has an online  $p_T^{GMT} \geq p_{T,TriggerThreshold}$ , has a quality<sup>viii</sup> of  $> 5$  or both a quality = 5 and  $BX^{ix}=0$ , is within  $|\eta| < 2.1$ , and is a radial distance of  $< 0.5$  in  $\eta$ - $\phi$  space from the probe. There is an added complication in that the online  $\phi$  value is calculated at the calorimeter while the offline  $\phi$  is calculated at the origin. When matching is performed, the offline  $\phi$  is extrapolated to the muon system in the algorithm (rather than the online value being extrapolated to the origin) in order to preserve the integrity of the online information<sup>x</sup>. Finally, the efficiency without isolation is shown in Figure 3.11 and is then defined as:

$$Efficiency = \frac{e_{match}}{e_{TP}}, \quad (3.3)$$

where  $e_{match}$  is the number of events that have a tag, a probe, and a GMT-probe match; and  $e_{TP}$  is the number of events that have a tag and a probe.

When isolation is used to lower the trigger rate, it must also be included in the efficiency calculation as an additional requirement for the (L1) GMT muon, influencing

---

<sup>viii</sup>Here, quality is used as a discrimination variable dependent on the impact parameter of the muon track, the normalized  $\chi^2$  of the fit of the track helix to the hits, and the number of hits used in the fit. More information can be found in references [43], [44], and [45].

<sup>ix</sup> $BX=0$  is used to signify that the muon candidate originated from the central, triggering, bunch crossing.

<sup>x</sup>The choice of maintaining the online information is the same logic as used in Section 3.4.1.2.

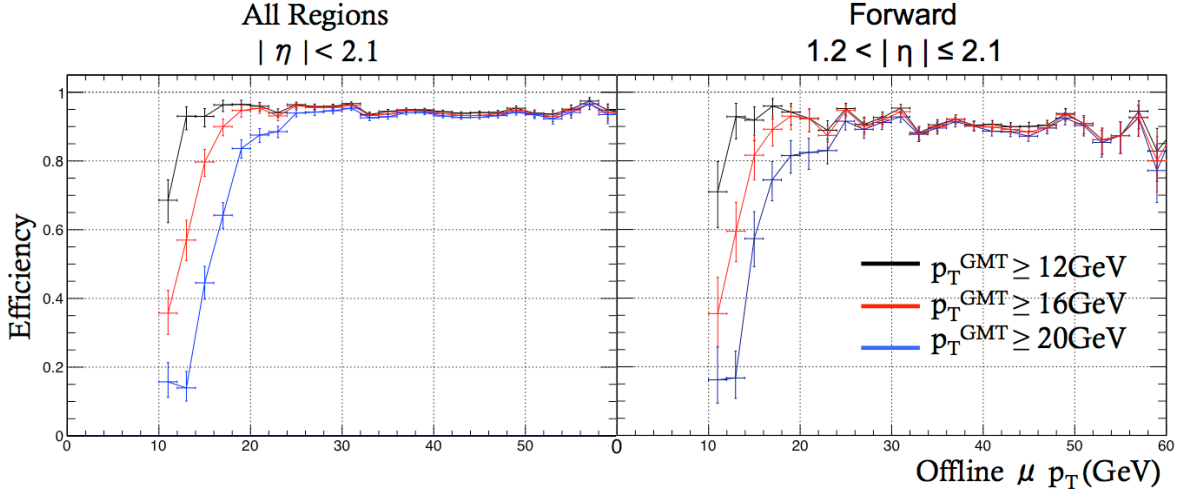


Figure 3.11 : The efficiency is calculated with Equation 3.3, and shown for three trigger  $p_T$  thresholds. The offline  $\mu$   $p_T$  corresponds to the matched probe  $p_T$ . The left plot shows the efficiency for all regions. The right plot shows the efficiency in the endcap region.

the numerator of Equation 3.3. Explicitly, the added isolation requirement is that the absolute or relative isolation region sum (Equation 3.2 and Equation 3.2 respectively) is less than a specified isolation cut. The relative efficiency is then a useful tool for determining, quantitatively, how significantly the efficiency is impacted by requiring a given GMT isolation cut, and is defined as:

$$Relative\ Efficiency = \frac{e_{WithIsolation}}{e_{NoIsolation}}, \quad (3.4)$$

where  $e_{WithIsolation}$  is the efficiency calculated with including an isolation requirement and  $e_{NoIsolation}$  is the efficiency without isolation (Equation 3.3). Since the denominator of Equation 3.3 is not altered by adding an isolation requirement, Equation 3.4 becomes:

$$\frac{e_{iso}}{e_{match}}, \quad (3.5)$$

where  $e_{iso}$  is the number of events that have a tag and a probe and a GMT-probe match and pass isolation.

### 3.6.2 Relative Rate

The trigger rate is the number of events that are recorded (or, trigger) per second. So, for any given event this is a binary quantity; either the event triggers, or it does not. The event will trigger if it passes the rate selection. The rate selection requires that an event contain at least one muon that:

1. meets the quality criteria
  - (a) a quality of  $> 5$
  - (b) or a quality = 5 and BX=0
2. has a  $p_T^{GMT} \geq p_{T,TriggerThreshold}$ ,
3. is within  $|\eta| < 2.1$  .

If these criteria are not met, then the event will not trigger, and therefore, does not add to the rate. Comparable to the relative efficiency (Equation 3.4) the relative rate is defined to determine how effective a given isolation cut is at reducing the trigger rate:

$$\text{Relative Rate} = \frac{r_{iso}}{r}, \quad (3.6)$$

where  $r_{iso}$  is the number of events with a muon that passes the rate selection and isolation; and  $r$  is the number of events with a muon that passes the rate selection.

### 3.6.3 Absolute Isolation Variable

The absolute isolation variable, given by Equation 3.2, is shown in Figure 3.12. As explained in Section 3.3, the rate information is derived from the minimum bias (MinBias) sample while the efficiency information is from the  $Z\mu\mu$  sample. For each data set, the absolute isolation variable is shown as calculated with  $E$  and  $E_T$  separately, and for full granularity regions with a radius of 0.4 in  $\eta$ - $\phi$  space and 3x3 RCT regions (12x12 tower sums in the barrel and scaling in  $\eta$ ). Since  $E$  and  $E_T$  only differ by a geometric factor<sup>xi</sup>, no physics is changed by choosing one over the other. However,  $E_T$  is a more useful and common quantity because it is Lorentz invariant to boosts in the z-direction. When performing algorithms to optimize the effectiveness of GMT muon isolation (lowering the rate significantly while minimizing a loss in efficiency), the quantity,  $E$  or  $E_T$ , is chosen based on the larger discrepancy between the  $Z\mu\mu$  and MinBias samples. For full granularity regions, it is determined from Figure 3.12 that  $E_T$  is a slightly better discriminant between the  $Z\mu\mu$  and MinBias samples. For the RCT regions, it is found that the  $E$  is a somewhat better discriminant between

---

<sup>xi</sup>Recall that  $E_T = E \sin(\theta)$ .

the two samples. Thus, in the remainder of this chapter, whenever absolute isolation is calculated,  $E_T$  is used for full granularity regions, while  $E$  is used for RCT regions.

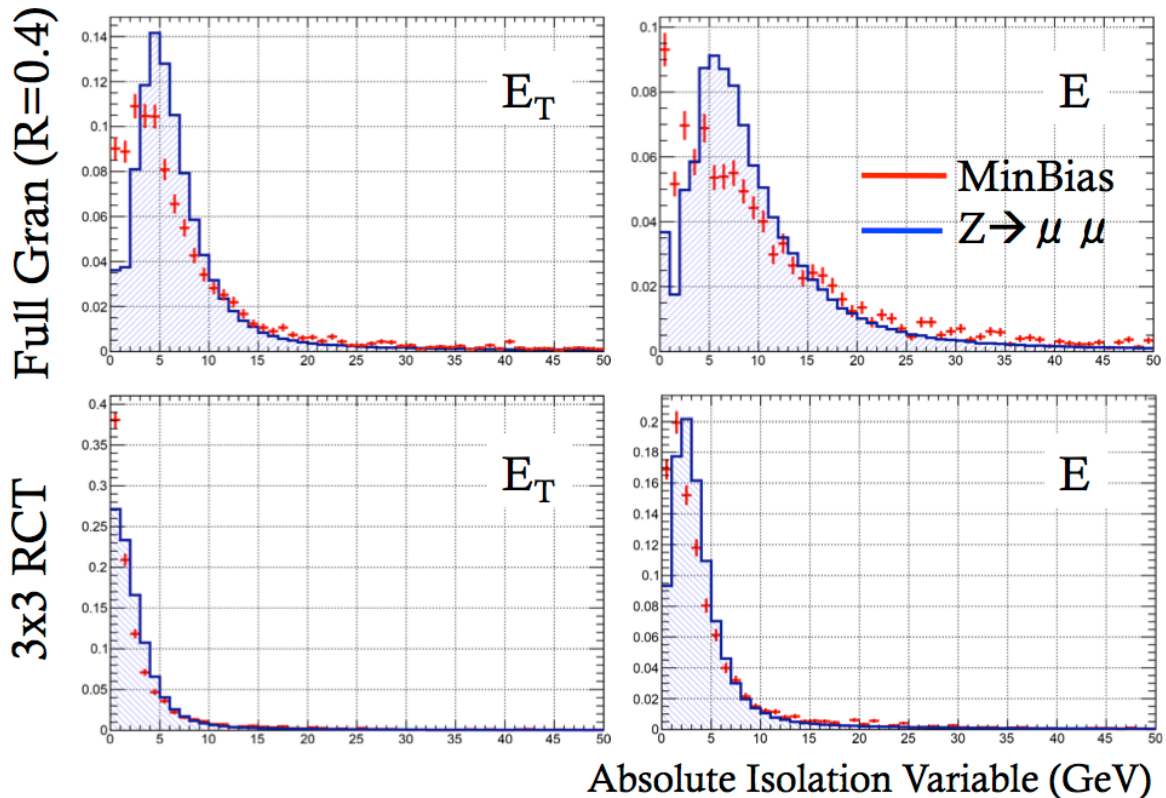


Figure 3.12 : Absolute isolation variable for 3x3 RCT regions and full granularity regions (radius=0.4 in  $\eta$ - $\phi$  space) are shown for the  $Z\mu\mu$  (blue line) and MinBias (red crosses) samples.  $E$  and  $E_T$  are shown separately for each region type.

### 3.6.4 Relative Isolation Variable

The relative isolation variable, given by Equation 3.2, is shown in Figure 3.13. The denominator of Equation 3.2 is the  $p_T$  of the GMT muon. However, since the true upgraded ( $\sim 2015$ ) trigger  $p_T$  resolution capabilities are unknown several cases are considered. The  $p_T^{GMT}$  represents the current ( $\sim 2014$ ) capabilities, and online muon

$p_T \geq$  trigger  $p_T$  threshold, is used in all cases (see Section 3.6.1 and 3.6.2) when required. The  $p_T^{SA}$  uses the offline standalone  $p_T$  and is used to simulate the best possible scenario with increased  $p_T$  resolution after the LS1 upgrades are complete. It is important to note that using the  $p_T^{SA}$  implies an offline match (where matching criteria are described in Section 3.6.1) to the online (GMT)  $\mu$  where the  $p_{T,online\mu}^{GMT} \geq$  trigger  $p_T$  threshold. Also, when using  $p_T^{SA}$ , the standalone muon  $p_T \geq$  trigger  $p_T$  threshold is used in all cases when required. Finally,  $p_T^{OFF}$  (perfect) uses the offline muon  $p_T$  and is used to show the absolute best (unrealistic) possible performance of GMT muon isolation. This is helpful in determining the general behavior of how the online  $p_T$  resolution affects the performance of isolation. When using  $p_T^{OFF}$ , the standalone muon  $p_T$  is used for the trigger  $p_T$  threshold, and the offline  $p_T$  is used when calculating the relative isolation.

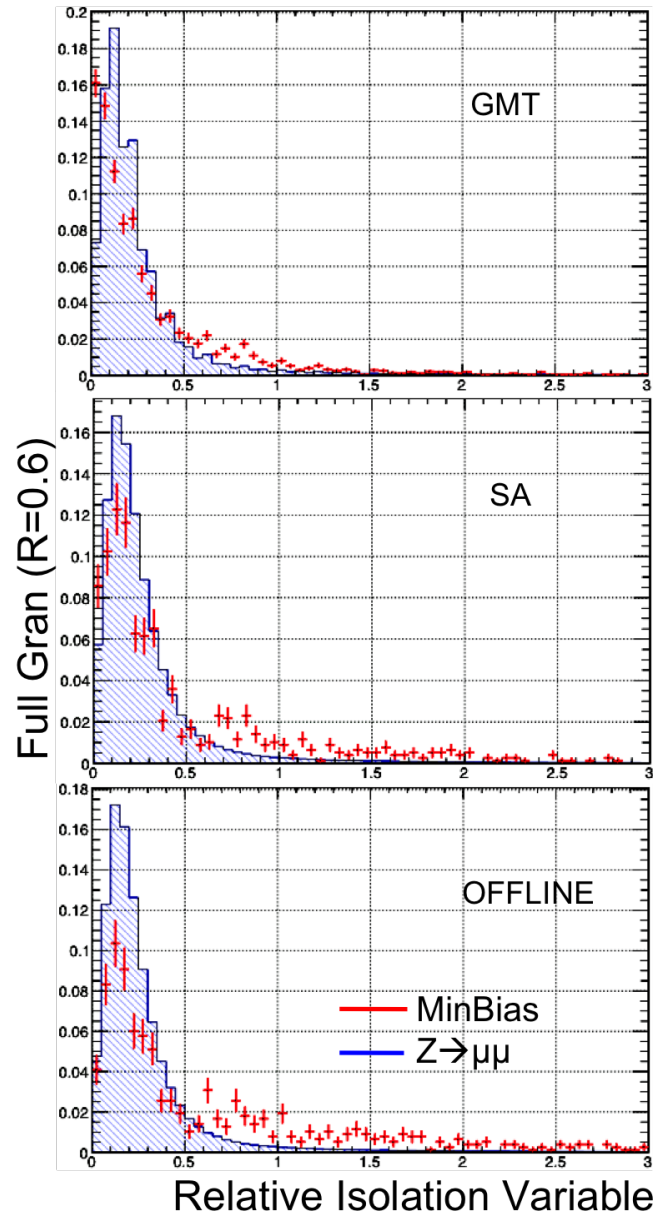


Figure 3.13 : Relative isolation variable for full granularity ( $R=0.6$  in  $\eta$ - $\phi$  space) is shown for three momentum resolutions. The  $Z\mu\mu$  (blue line) and MinBias (red crosses) are shown for each case.

### 3.7 Results of GMT Muon Isolation

Results are presented, mainly, in the form of “rate of change” (ROC), relative efficiency vs relative rate, plots. Each point on the ROC curves corresponds to a specific isolation cut where relative or absolute isolation will be specified. Also specified will be the  $|\eta|$  region covered by each plot, the  $p_T$  resolution, and the region size. As stated in Section 3.6.3  $E_T$  will be used for all full granularity regions, and  $E$  will be used for all RCT region isolation calculations.

Figure 3.14 is the ROC plot for both relative and absolute isolation for full granularity regions of varying radius, including the full  $\eta$  range ( $|\eta| < 2.1$ ), using GMT momentum resolution, and a trigger  $p_T$  threshold of  $p_T^{GMT} \geq 12\text{GeV}$ . It is immediately obvious for both relative and absolute isolation that increasing the isolation region radius reduces the rate by more with a smaller loss of efficiency, but this effect begins to plateau. Specifically, the increased rate reduction for a given isolation cut is larger between  $R=0.4$  to  $R=0.6$  than from  $R=0.6$  to  $R=0.8$ . However, as the region radius goes to infinity, the effect of isolation goes to zero. Similarly, muon isolation loses effectiveness (and significance) as the region radius goes to zero. Furthermore, relative isolation reduces the rate by more than the absolute isolation for the same loss of efficiency. Additionally for  $R=0.4$  and absolute isolation, the efficiency drops faster than the rate. This expresses the fact that for a small isolation radius the physical region area in the high  $\eta$  region is too small for isolation to be effective and meaningful.

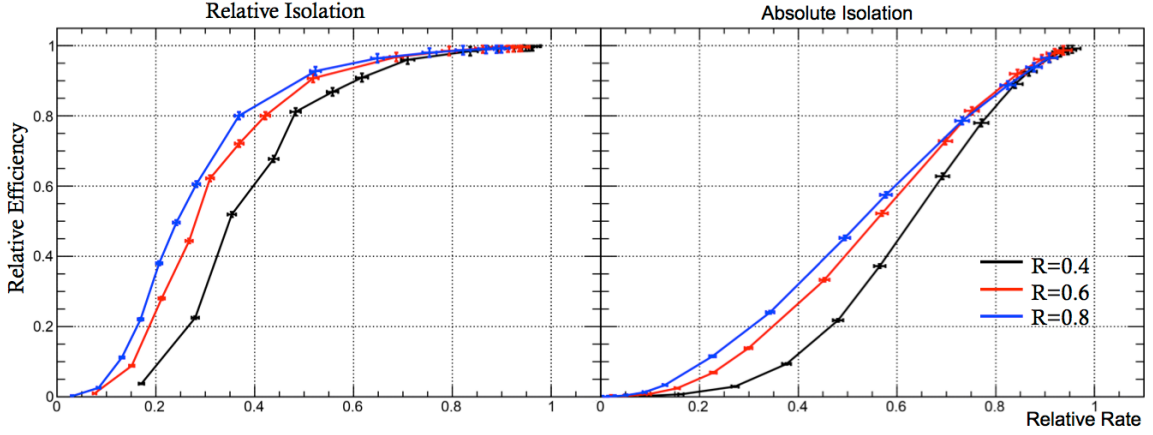


Figure 3.14 : Rate of change plots of full granularity regions of varying radius for both relative (left) and absolute (right) isolation.  $|\eta| < 2.1$  and  $p_T^{GMT} \geq 12\text{GeV}$  used for momentum thresholds.

Figure 3.15 is a ROC plot comparing the effectiveness of full granularity and RCT regions. Assorted region areas are shown for the entire  $\eta$  range ( $|\eta| < 2.1$ ), and GMT  $p_T$  resolution ( $p_T^{GMT} \geq 12\text{GeV}$  for the trigger  $p_T$  threshold) is used. In the barrel region, a full granularity region with  $R=0.4$  is about the same physical size as a  $3 \times 3$  RCT region. However, since the RCT regions scale with  $\eta$ , this is not consistent throughout the detector. A  $5 \times 5$  RCT region is much larger than a full granularity region with a radius of 0.6 throughout all regions in the detector. For (approximately) equivalently sized regions, full granularity regions are always more effective at reducing the rate while maintaining efficiency compared to the RCT regions. This is to be expected since the full granularity regions are more precisely positioned about the incident muon energy deposition in the calorimeter. For the reason of positioning, even-valued ( $2 \times 2$ ,  $4 \times 4$ , etc.) RCT regions are not considered since this would require an arbitrary choice of where to center the region. The plateau effect is also present

and becomes apparent for larger region sizes.

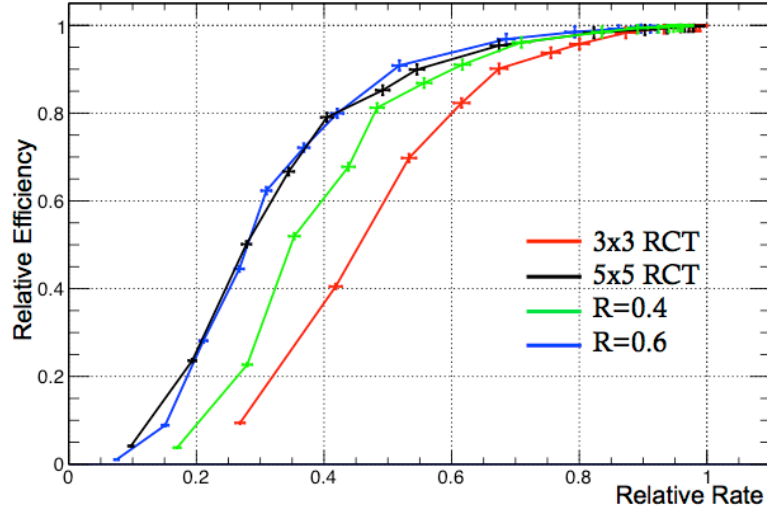


Figure 3.15 : Rate of change plot of full granularity and RCT regions of varying size for relative isolation.  $|\eta| < 2.1$  and  $p_T^{GMT} \geq 12\text{GeV}$  used for momentum thresholds.

Figure 3.16 shows ROC plots for relative isolation using full granularity regions with a radius of 0.6, showing each  $\eta$  separately, and using  $p_T^{GMT}$  for varying trigger  $p_T$  thresholds. The overall behavior of the curves are consistent over all  $\eta$  regions even though the full granularity regions do not scale with  $\eta$ . Isolation performs best in the barrel region and slightly worse in the forward and overlap regions. Also, although the relative rate is drastically affected by the trigger  $p_T$  threshold, the relative efficiency is not. This is apparent since for any given trigger  $p_T$  threshold, the plot points do not show vertical dissimilarities. This is because when the event selection is performed to calculate the efficiency the invariant mass cut on the muons ( $91 \pm 15$  GeV) almost guarantees that both muons are within the plateau region of the efficiency without

isolation<sup>xii</sup>, shown in Figure 3.11. The relative rate is impacted, however, because it is not subject to this event selection. Thus, lowering the trigger  $p_T$  threshold allows more events to be triggered, and these events are easy to eliminate using isolation, hence lowering the relative rate significantly.

The impact of the  $p_T$  resolution is now seen by the ROC plots in Figure 3.17. Each plot is for full granularity regions with a radius of 0.6, includes all values of  $\eta$  ( $|\eta| < 2.1$ ), and varying trigger  $p_T$  threshold and  $p_T$  resolution. As expected from the isolation variable plots, Figure 3.13,  $p_T^{OFF}$  is more effective than  $p_T^{SA}$ , which is more effective than  $p_T^{GMT}$ . As noted in Section 3.6.4, it is important to recall that for the  $p_T^{OFF}$  curves, the  $p_T^{SA}$  is used for the trigger  $p_T$  threshold and the offline  $p_T$  is used for calculating the relative isolation.

Also in Figure 3.17, it can be seen that there is an efficiency dependence on the  $p_T$  resolution. For a given isolation cut, the  $p_T^{OFF}$  and  $p_T^{SA}$  have (about) the same relative efficiency while the  $p_T^{GMT}$  curves have a higher relative efficiency. This is because when using both the offline and standalone resolutions, it has been implicitly required that an online match exist.

Figure 3.18 shows ROC plots of full granularity regions ( $R=0.6$ ) with varying  $p_T$

---

<sup>xii</sup>As a rule of thumb, the plateau region of the efficiency is typically  $\sim 8$  GeV above the trigger  $p_T$  threshold.

resolutions with a constant trigger  $p_T$  threshold of  $\geq 20$  GeV, using relative isolation where  $\eta$  is delineated by detector region. Using all of the previous results, it is clear that the barrel and overlap regions behave as expected. Yet, in the endcap region, increasing the  $p_T$  resolution from  $p_T^{GMT}$  to  $p_T^{SA}$  has a minimal effect on the behavior. This raises the question: since the  $p_T^{SA}$  and  $p_T^{OFF}$  algorithms only differ in the calculation of the relative isolation variable (the denominator of Equation 3.2), why does the  $p_T^{OFF}$  curve reduce the rate by so much more for the same loss of efficiency as the  $p_T^{SA}$  and  $p_T^{GMT}$  curves?

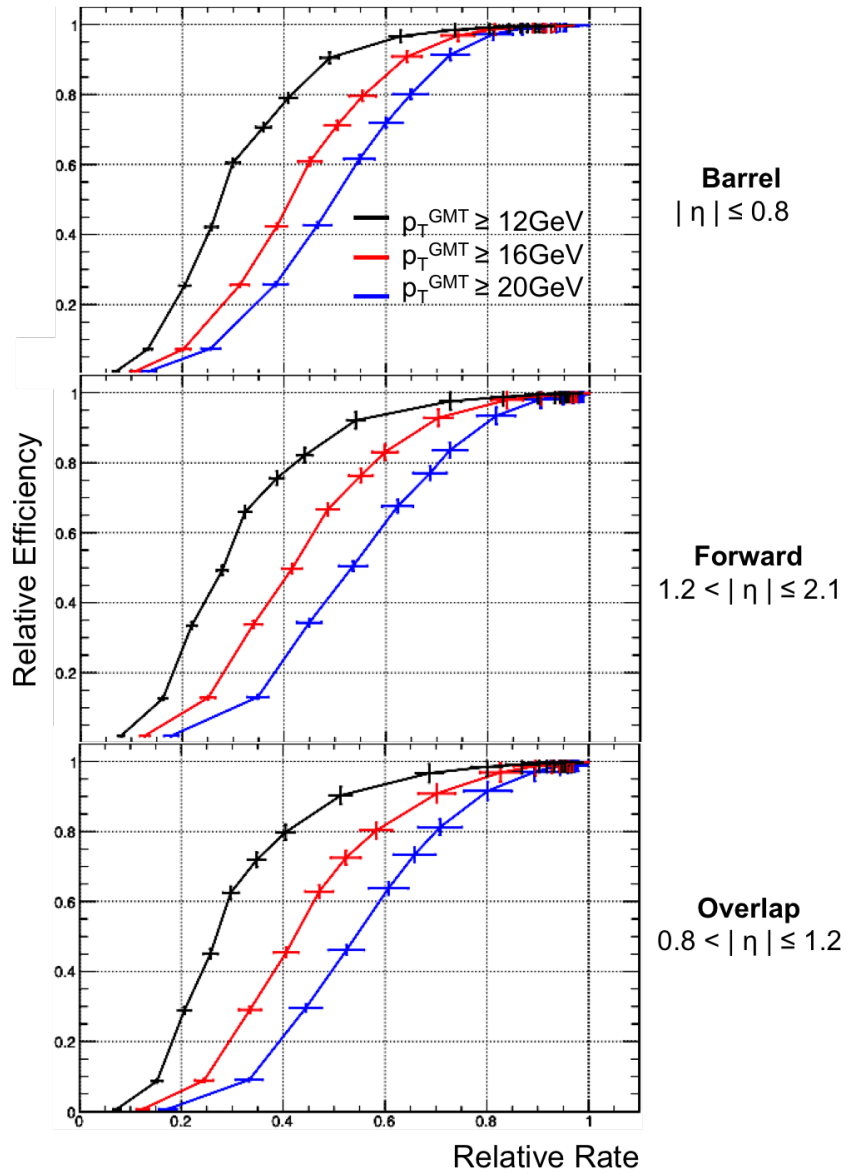


Figure 3.16 : Rate of change plots of full granularity regions ( $R=0.6$ ) with varying  $p_T^{GMT}$  trigger  $p_T$  threshold using relative isolation.  $|\eta|$  delineated by detector region.

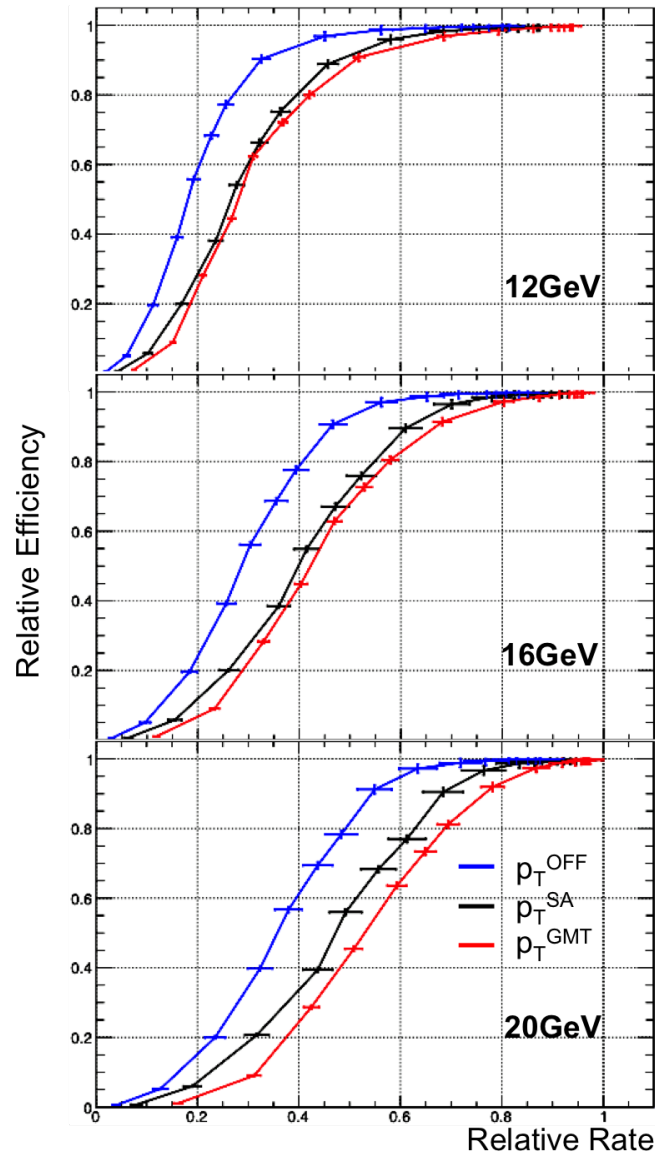


Figure 3.17 : Rate of change plots of full granularity regions ( $R=0.6$ ) with varying  $p_T$  trigger  $p_T$  threshold and resolution using relative isolation.  $|\eta| < 2.1$ .

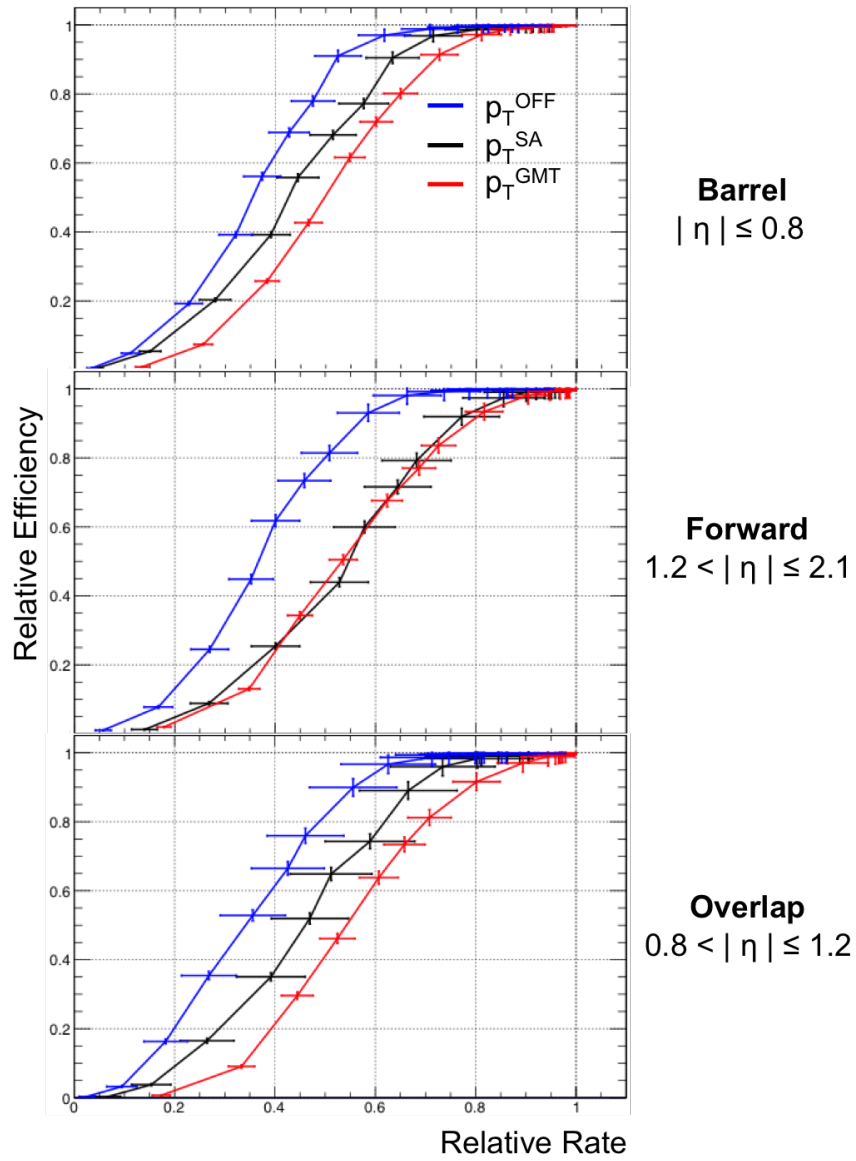


Figure 3.18 : Rate of change plots of full granularity regions ( $R=0.6$ ) with varying  $p_T$  resolution, a trigger  $p_T$  threshold of  $\geq 20$  GeV, using relative isolation.  $|\eta|$  delineated by detector region.

### 3.7.1 Explanation of Endcap Behavior

In order to explain why the rate is reduced by  $\sim 20\%$  more in the endcap region for the  $p_T^{OFF}$  resolution compared to the  $p_T^{GMT}$  and  $p_T^{SA}$  (see Figure 3.18) the  $p_T$  distribution must be examined for each resolution. Figure 3.19 shows the  $p_T$  distribution for each resolution for muons with isolation (using full granularity regions with a radius of 0.6, a trigger  $p_T$  threshold of 20 GeV, and an isolation cut of 0.25) and muons without requiring isolation. The particular isolation cut is only important insofar as it is the same for all resolutions. A “suspicious” region is marked on the  $p_T^{OFF}$  distribution and contains  $\sim 25\%$  of the rate. This region is suspect because these are muons which have a  $p_T$  below the trigger  $p_T$  threshold and, therefore, do not appear in the GMT or SA resolution plots. Further, the muons in the suspicious region are not isolated, and so diminish the relative rate by about  $\sim 20\%$  overall when isolation is applied. It is then necessary to verify the behavior seen in the suspicious region. Figure 3.20 shows the  $p_T^{SA}$  residual defined as:

$$p_T^{SA} \text{ Residual} = \frac{p_T^{SA} - p_T^{OFF}}{p_T^{OFF}}. \quad (3.7)$$

Since the  $p_T^{OFF}$  is the highest resolution available, the  $p_T^{SA}$  residual can be used to check the accuracy of the  $p_T^{SA}$ . Figure 3.20 (left) shows the residual over all detector regions ( $|\eta| < 2.1$ ) for all muons. This shows a very good correlation between the SA and OFF resolutions, but has a long tail. The right histogram shows only the  $p_T^{SA}$  residual for the suspicious region ( $(p_T^{SA} > 20 \text{ GeV}, p_T^{OFF} < 20 \text{ GeV}, 1.2 < |\eta| < 2.1)$ ), and

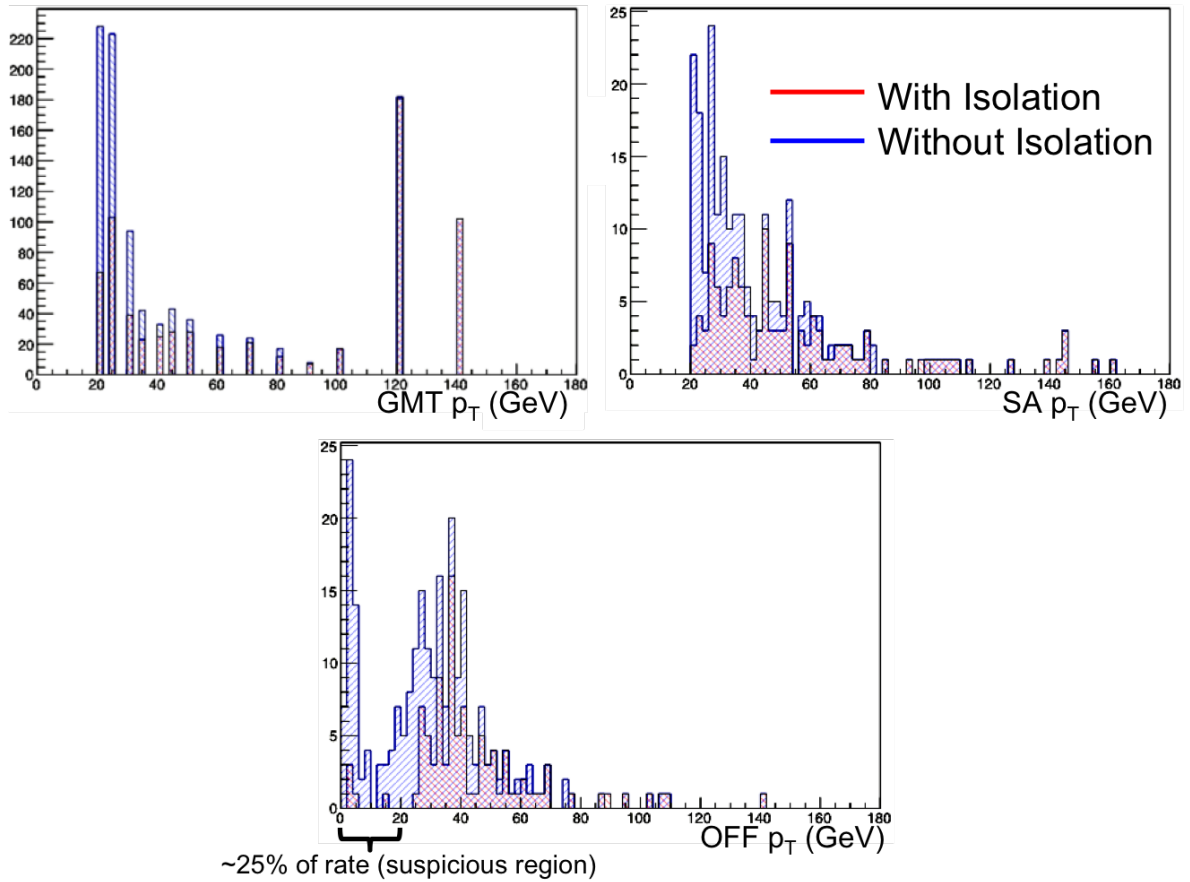


Figure 3.19 :  $p_T$  distributions of muons with and without isolation requirements. Isolation is calculated with full granularity regions ( $R=0.6$ ), a  $p_T$  threshold of 20 GeV, and an isolation cut of 0.25. The “suspicious” region is shown in the  $p_T^{OFF}$  distribution.

a very poor correlation is seen. It may then be concluded that the muons in the suspicious region must be located in the tail of the histogram shown in Figure 3.20 (left).

Thus, because  $\sim 20\%$  of the muons have poor  $p_T^{SA}$ - $p_T^{OFF}$  agreement in the endcap, the trigger  $p_T$  threshold is less effective when using the  $p_T^{OFF}$  for relative isolation because of the GMT-offline matching. This means that muons that should have

been eliminated by the trigger  $p_T$  threshold cut (in the suspicious region) are being eliminated instead by the relative isolation cut, causing the relative rate to drop dramatically. This explains why the curve in Figure 3.18 for the  $p_T^{OFF}$  does much better at reducing the rate for a given loss of efficiency than the  $p_T^{SA}$  and  $p_T^{GMT}$  curves.

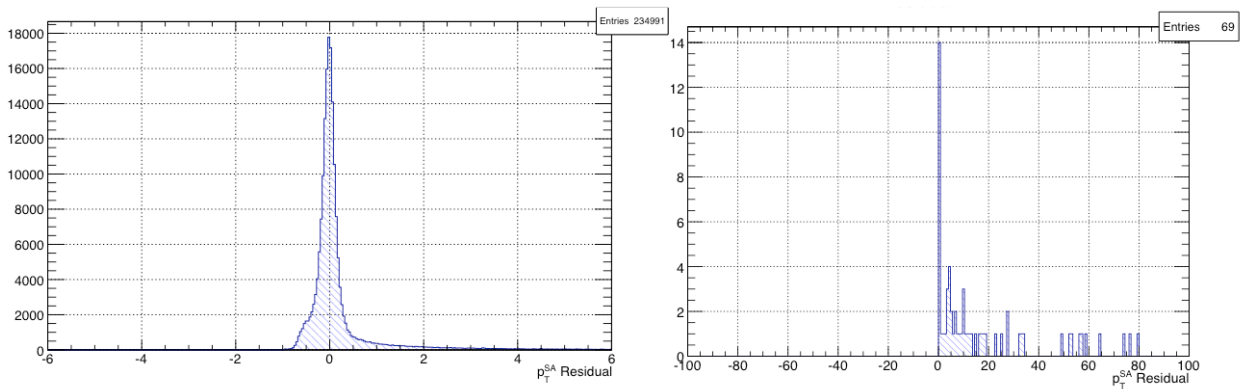


Figure 3.20 : The  $p_T^{SA}$  residual (Equation 3.7). Left shows residual for all muons ( $|\eta| < 2.1$ ). Right shows residual for muons in the suspicious region ( $p_T^{SA} > 20$  GeV,  $p_T^{OFF} < 20$  GeV,  $1.2 < |\eta| < 2.1$ ).

### 3.7.2 Effects of Isolation on Efficiency ( $|\eta| \leq 2.1$ )

The effects of GMT muon isolation on the efficiency is studied in detail in order to get a sense of the practical application of GMT muon isolation. The following results all use full granularity regions ( $R=0.6$ ) and use muons from all areas of the detector ( $|\eta| \leq 2.1$ ). A trigger  $p_T$  threshold of  $\geq 16$  GeV is used for all chosen isolation cut points. Figure 3.21 shows how the efficiency curve is affected by using the circled isolation point from the ROC plot, for GMT  $p_T$  resolution. The efficiency is shown to

be diminished for low  $p_T$  muons. The same effect is seen if SA  $p_T$  resolution is used as shown in Figure 3.22. However, when the SA resolution is used, the efficiency is diminished by less than the GMT resolution for low  $p_T$  muons.

Figure 3.23 and Figure 3.24 show the corresponding absolute isolation results under the same conditions. In contrast to the relative isolation, the absolute isolation uniformly reduces the efficiency for muons of all  $p_T$ . Again, this effect is less severe when using the SA  $p_T$  resolution compared to the GMT  $p_T$  resolution.

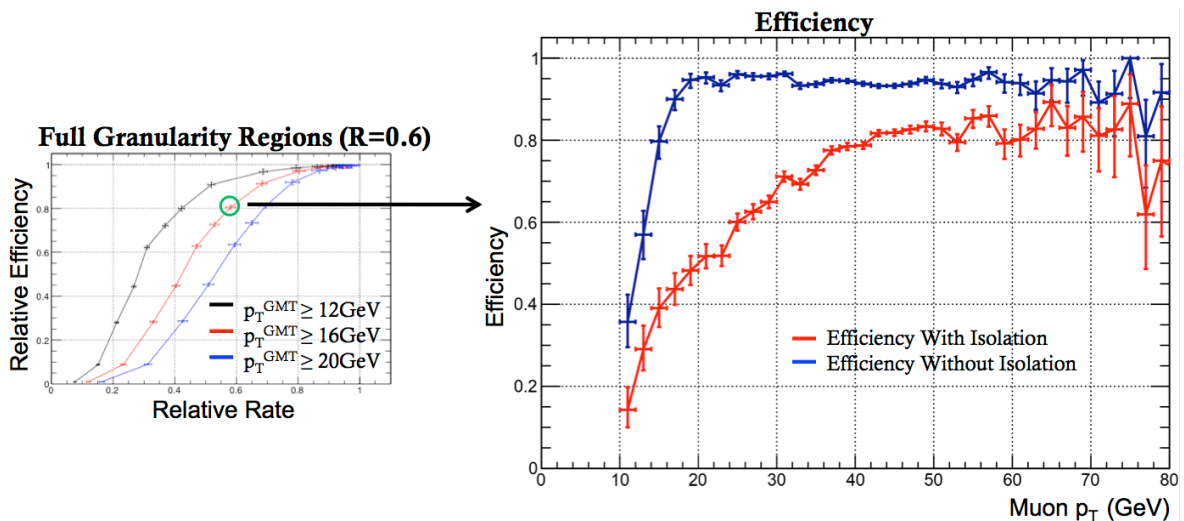


Figure 3.21 : The left ROC plot is for full granularity regions ( $R=0.6$ ) with GMT  $p_T$  resolution, a varying trigger  $p_T$  threshold, using relative isolation ( $|\eta| < 2.1$ ). The right plot shows the efficiency without isolation, and the efficiency for the circled point in the left plot.

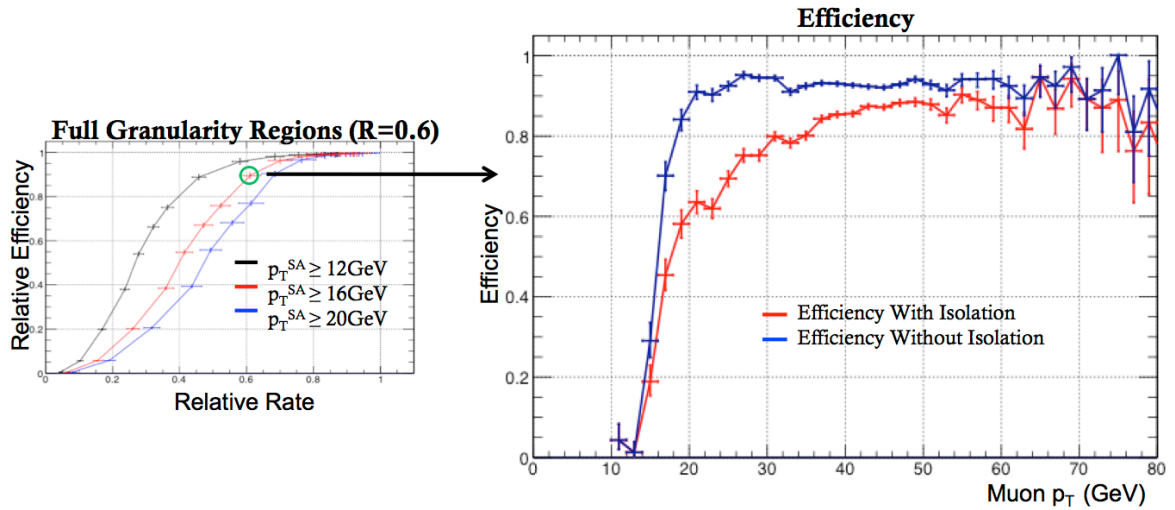


Figure 3.22 : The left ROC plot is for full granularity regions ( $R=0.6$ ) with SA  $p_T$  resolution, a varying trigger  $p_T$  threshold, using relative isolation ( $|\eta| < 2.1$ ). The right plot shows the efficiency without isolation, and the efficiency for the circled point in the left plot.

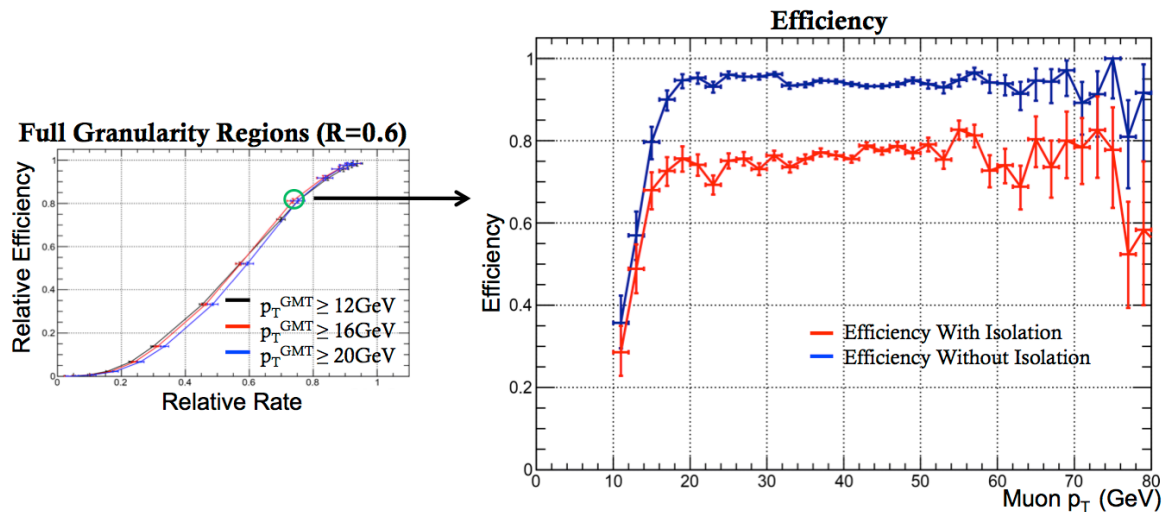


Figure 3.23 : The left ROC plot is for full granularity regions ( $R=0.6$ ) with GMT  $p_T$  resolution, a varying trigger  $p_T$  threshold, using absolute isolation ( $|\eta| < 2.1$ ). The right plot shows the efficiency without isolation, and the efficiency for the circled point in the left plot.

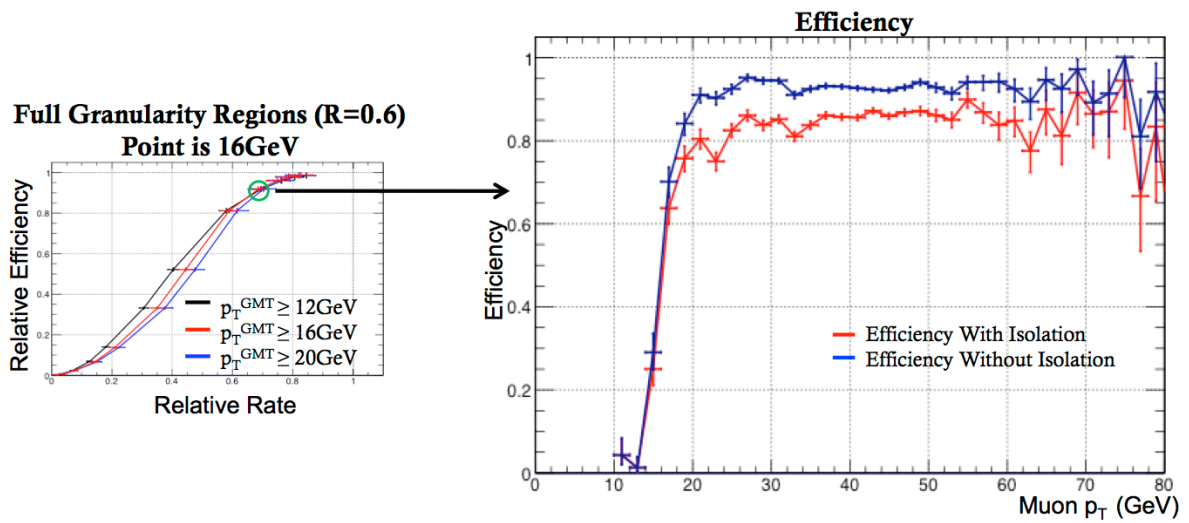


Figure 3.24 : The left ROC plot is for full granularity regions ( $R=0.6$ ) with GMT  $p_T$  resolution, a varying trigger  $p_T$  threshold, using absolute isolation ( $|\eta| < 2.1$ ). The right plot shows the efficiency without isolation, and the efficiency for the circled point in the left plot.

### 3.7.3 Effects of Isolation on Efficiency in Endcap ( $1.2 < |\eta| \leq 2.1$ )

The effects of the GMT muon isolation on the efficiency in the endcap ( $1.2 < |\eta| \leq 2.1$ ) is now studied in further detail. All of the following results use the same conditions and are comparable to the results of Section 3.7.2: full granularity regions ( $R=0.6$ ) and a chosen trigger  $p_T$  threshold of  $\geq 16$  GeV is used. Figure 3.25 and Figure 3.26 show the efficiency of a specific (circled) isolation cut for GMT  $p_T$  resolution and SA  $p_T$  resolution respectively. Again, the efficiency is diminished for low  $p_T$  muons, which is the same behavior seen in the entire  $\eta$  range. Again, the SA resolution shows a slight increase in performance when compared to the GMT resolution. Figure 3.27 and Figure 3.28 show the corresponding results using absolute isolation. Analogous to the entire  $\eta$  range, the efficiency is uniformly reduced for all  $p_T$  muons. The benefit of the increased  $p_T$  resolution does not seem to have a large impact, and the SA and GMT resolutions perform equivalently.

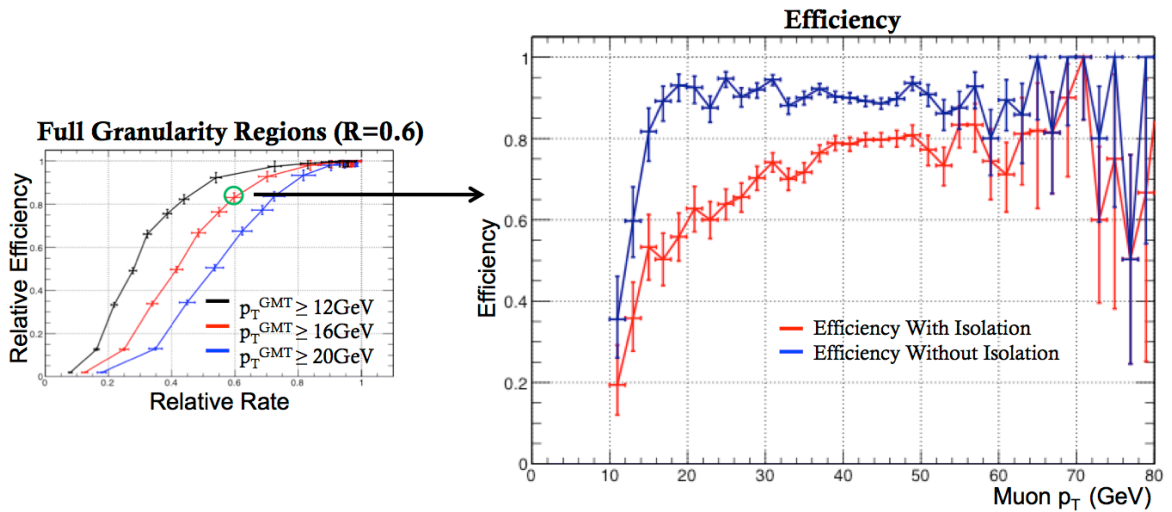


Figure 3.25 : The left ROC plot is for full granularity regions ( $R=0.6$ ) with GMT  $p_T$  resolution, a varying trigger  $p_T$  threshold, using relative isolation ( $1.2 < |\eta| \leq 2.1$ ). The right plot shows the efficiency without isolation, and the efficiency for the circled point in the left plot.

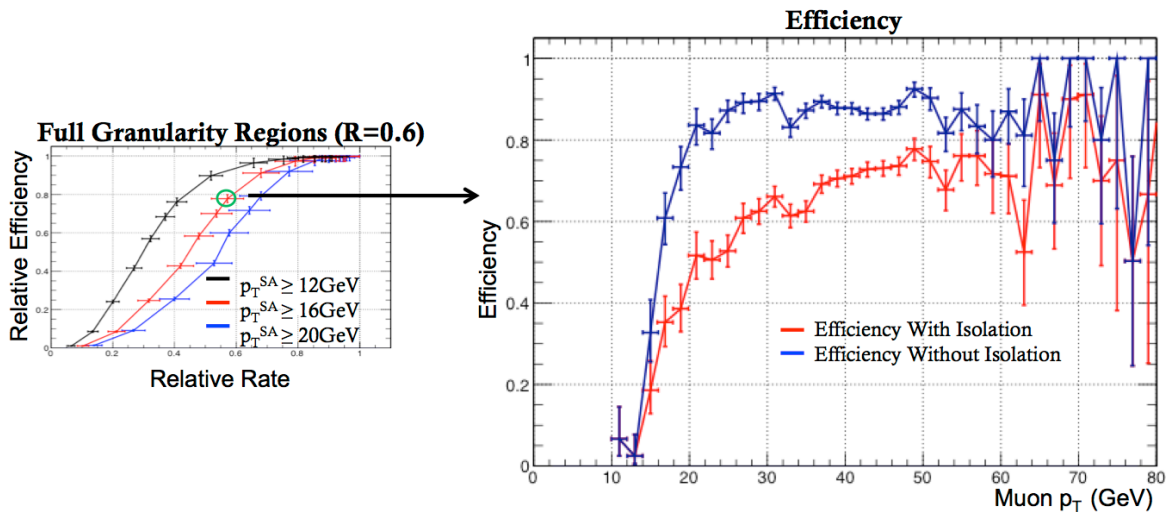


Figure 3.26 : The left ROC plot is for full granularity regions ( $R=0.6$ ) with SA  $p_T$  resolution, a varying trigger  $p_T$  threshold, using relative isolation ( $1.2 < |\eta| \leq 2.1$ ). The right plot shows the efficiency without isolation, and the efficiency for the circled point in the left plot.

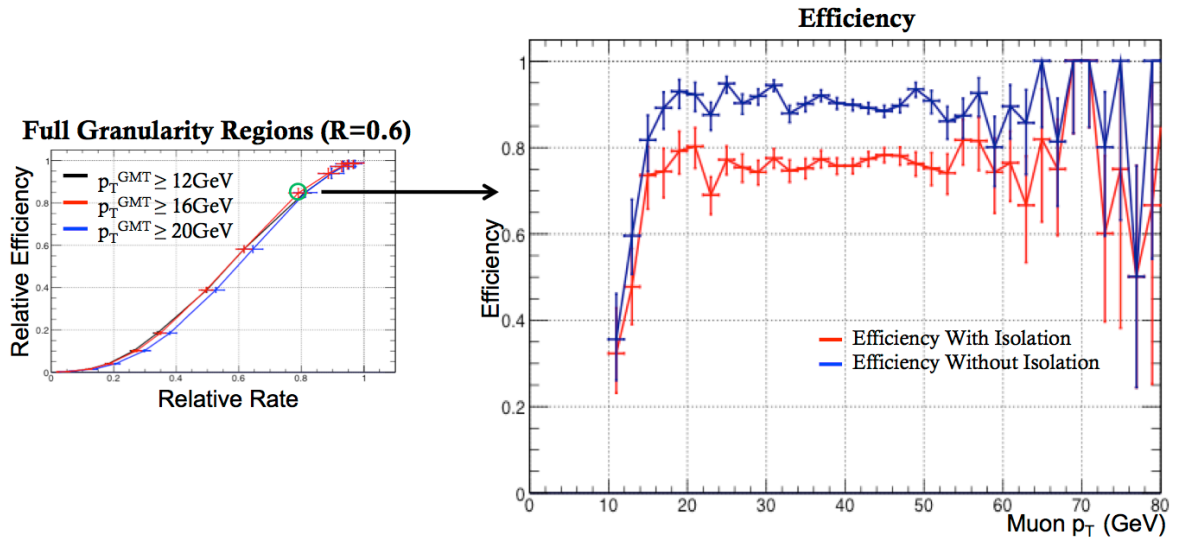


Figure 3.27 : The left ROC plot is for full granularity regions ( $R=0.6$ ) with GMT  $p_T$  resolution, a varying trigger  $p_T$  threshold, using absolute isolation ( $1.2 < |\eta| \leq 2.1$ ). The right plot shows the efficiency without isolation, and the efficiency for the circled point in the left plot.

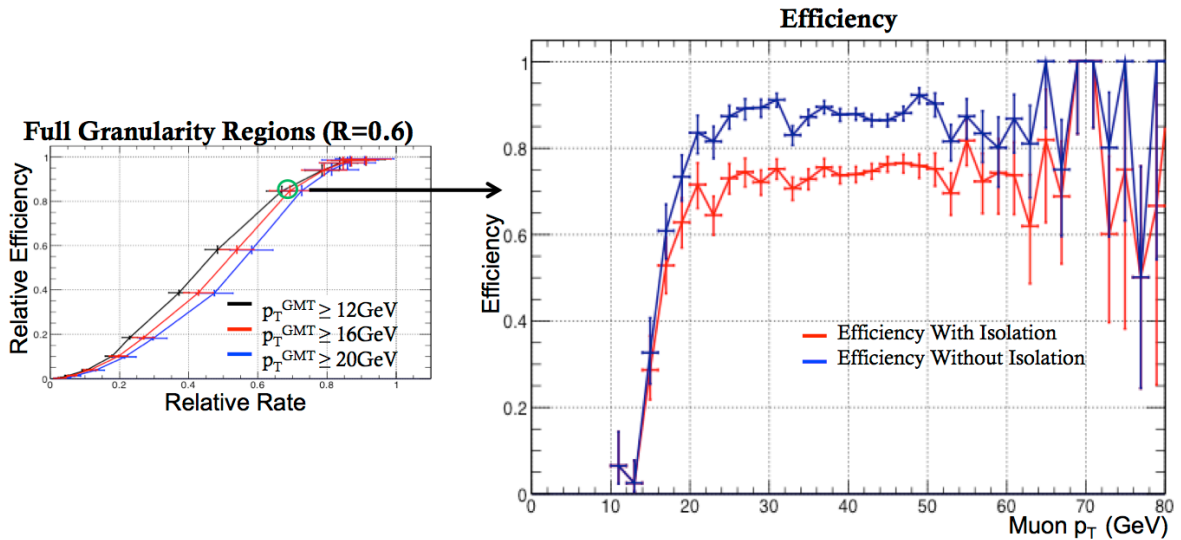


Figure 3.28 : The left ROC plot is for full granularity regions ( $R=0.6$ ) with SA  $p_T$  resolution, a varying trigger  $p_T$  threshold, using absolute isolation ( $1.2 < |\eta| \leq 2.1$ ). The right plot shows the efficiency without isolation, and the efficiency for the circled point in the left plot.

### 3.8 Summary

From the results of Section 3.7, it can be concluded that for GMT muon isolation, full granularity regions are always better than RCT regions at reducing the rate while maintaining efficiency. Further, although relative isolation appears to be more effective than absolute isolation at reducing the rate with a lower loss of efficiency, in reality, the relative isolation kills the efficiency turn-on curve and effectively changes the  $p_T$  trigger threshold. Using absolute isolation is better for low  $p_T$  muons, but reduces the efficiency uniformly for all  $p_T$  muons. Absolute isolation, in essence, acts as a pre-scale (meaning that events are thrown away at random). Therefore, relative isolation is preferable to absolute isolation for GMT muon isolation because it is unacceptable to lose efficiency in the high  $p_T$  region.

Additionally, from Figure 3.16 it can be seen that increasing the  $p_T$  resolution will directly benefit all regions of the detector other than the endcap. Applying GMT muon isolation could lower the rate by  $\sim 10\%$  without a noticeable drop in efficiency as shown in Figure 3.17. It should be noted that increasing the  $p_T$  resolution appears to have a secondary effect: it helps to steepen the efficiency turn-on curve. This means that low  $p_T$  muons are most affected by the gain in efficiency from the increased  $p_T$  resolution.

The use of GMT muon isolation alone as proposed in this study is not a sufficiently

effective method of controlling the rate while maintaining efficiency in the endcap region. This is because the relative isolation acts as a momentum dependent pre-scale, while the absolute isolation effectively removes events at random. However, the upgraded GMT system will include full granularity isolation region capabilities that will be implemented in conjunction with other techniques in order to lower the L1 rate while maintaining efficiency.

## Chapter 4

### **Radiation Testing of the Spartan-6 Programmable Device for the CSC Upgrade**

As described in 2.2.4.1, the Muon Port Card (MPC) selects the 3 best LCTs and sends them to the Track Finder (TF) crate (which is where the Muon Sorter (MS) resides). During LS1, the MPC mezzanine board will be replaced. The upgraded board will incorporate a new field-programmable gate array (FPGA) which will allow up to 18 LCTs to be sent to the Sector Processor (SP), and then on to the MS, every bunch crossing (25ns after LS1). This is a vast improvement over the current MPC.

The ability to consider more LCTs per MPC will allow for new physics to be studied in addition to providing more and better muon candidates to the CSCTF. New physics that may be studied as a consequence of the upgraded MPC mezzanine include lepton jets and other exotic processes which have signatures involving 4 or more closely spaced muons (which would, obviously, require at least 4 LCTs to be sent from the same MPC). Furthermore, additional muon trigger tracks may benefit triggering algorithms, such as GMT muon isolation.

When implementing new electronics in the CMS muon endcap system, unique con-

siderations need to be taken in to account. Endcap electronics in the CMS muon system at the CERN LHC are exposed to high levels of radiation during normal operation. Once all of the upgrades have been completed ( $\sim 2025$ ) the instantaneous luminosity will be five times higher than the current luminosity, and the expected levels of radiation received by the electronics is also expected to increase by a factor of  $\sim 5$ . Note that the LHC receives the title of “High-Luminosity LHC” (HL-LHC) after all currently planned upgrades are complete, which is expected in  $\sim 2025$ . In order to ensure that the Cathode Strip Chamber (CSC) MPC will continue to operate efficiently and accurately in the increased radiation environment, radiation testing of the proposed electronics must be performed [25].

## 4.1 Introduction

There are 540 endcap muon CSC chambers (after the addition of ME4/2 during LS1) arranged in four muon endcap (ME) stations at varying  $\eta$ . ME1/1 is located at the highest  $\eta$  and it is, therefore, expected to receive the highest levels of radiation. The MPCs are located inside of a VME crate on the periphery of the return yokes of the CMS detector. Since the MPCs are located outside of the detector, the expected radiation exposure will be much lower than that of the ME1/1 station. Thus, by considering the expected radiation exposure of the ME1/1 station as the baseline to measure acceptable electronic component efficiencies a safety factor of 3 is inherently

included [46]. Figure 4.1 (left) shows the neutron energy spectrum exposure in the ME1/1 region based on simulation from the first phase of LHC operation [47]. Figure 4.1 (right) shows the neutron fluence in the endcap region ME1 as a function of radius [47]. For 10 years of normal LHC operation, it has been determined from simulation that, the total ionizing dose of  $E > 100$  keV in the ME1/1 region is 1780 rad and the total neutron fluence is about  $6 \times 10^{11} \text{cm}^{-2}$  [47]. These rates are expected to increase by a factor of five for 10 years of HL-LHC operation and can be found in Table 4.1.

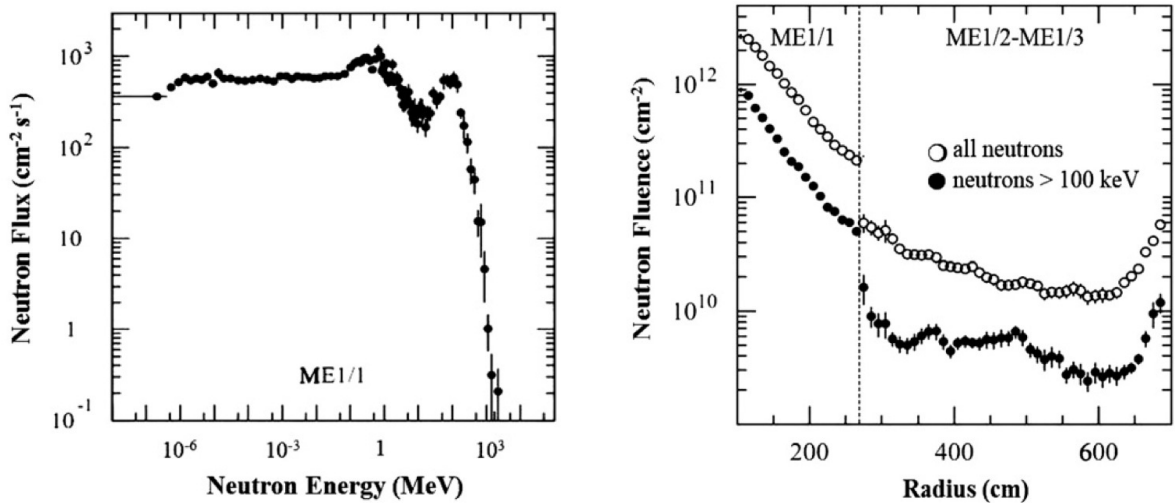


Figure 4.1 : Left plot shows the neutron energy spectrum exposure in the ME1/1 region. Right plot shows the neutron fluence as a function of radius in ME1/1, ME1/2, and ME1/3. ME1/1 has the highest radiation exposure and is delineated by a vertical dashed line. [48]

<b>Ten year HL-LHC exposure in ME1/1</b>	
<b>20 MeV neutron fluence</b>	$2.7 \times 10^{11} \text{ n/cm}^2$
<b>1 MeV neutron fluence</b>	$3.0 \times 10^{12} \text{ n/cm}^2$
<b>Total ionizing dose</b>	<b>8.9 krad</b>

Table 4.1 : Expected neutron exposure in 10 years of HL-LHC operation in the ME1/1 region. [48]

The commercial off-the-shelf Xilinx Spartan-6 XC6SLX150T programmable device for use in the upgraded MPC underwent an irradiation test by using a 64 MeV proton beam at the Crocker Nuclear Laboratory at the University of California, Davis (UCD). Note that during LHC operation, negative effects of radiation on electronics are expected to be caused by neutron interactions. In order to compensate, we assumed strong isospin symmetry and used the conversion factor of 1 krad of the proton beam radiation being equivalent to a neutron fluence of  $\sim 8 \times 10^9 \text{ cm}^{-2}$  [49]. However, since negative effects on the electronics from radiation in the HL-LHC environment is expected to be caused by  $> 20$  MeV neutrons, the response from protons and neutrons at these energies will be equivalent [50]. During testing, the device was exposed to a 30 year equivalent level of radiation expected in the ME1/1 environment. Note that the MPC is housed in a peripheral crate (as opposed to on the CSC chamber itself), so the radiation exposure to the MPC is expected to be less than the radiation received by ME1/1 by a factor of 3. Single Event Upsets (SEUs) (see Section 4.2 for details) were recorded, and damage from permanent and cumulative effects were considered. Our results show that the Spartan-6 XC6SLX150T will operate reliable

in the expected CMS endcap radiation environment.

## 4.2 Effects of Radiation on Electronics

### 4.2.1 SEUs

Temporary effects of the radiation on the MPC electronics were measured by exposing the electronics to known levels of radiation and recording the number of SEUs. An SEU occurs when radiation causes a hadronic interaction within the circuit to take place, a bit flip, that then changes the logical state of the circuit. There are two types of SEUs, which would cause errors while in use at the HL-LHC, and manifest themselves in four ways. The most common SEU is a single bit flip, which is self-recoverable, and is seen as a single error count. The other SEU type is when the pipeline chain or reset circuitry becomes broken and the FPGA must be reset. This SEU is indicated when large numbers of bit flips are continuously counted, a single large number of bit flips is simultaneously counted, or the FPGA freezes. These SEUs cause no permanent damage to the Spartan-6 FPGA. In the upgraded LHC operation it is expected that 90% of these upsets will be caused by neutrons with  $> 20$  MeV [50].

### 4.2.2 Permanent Damage

Other errors, which can accumulate and cause permanent damage, are also possible. These include latchup, when a large increase of current is drawn by a component and overheating of the silicon elements can occur; and incremental damage, which is attributed to a slow degradation of the silicon circuits by ionizing radiation [51]. Such effects would necessitate replacement parts, cause inconsistent reliability, and would therefore make a device unsuitable for use in the CSC MPC.

## 4.3 Radiation Testing Setup

The radiation testing setup is such that the Spartan-6 XC6SLX150T FPGA is mounted on the MPC mezzanine board, as shown in Figure 4.2 (left), and then placed in a modified VME crate perpendicular to the Crocker Nuclear Laboratory cyclotron beam, Figure 4.2 (right). The cyclotron provided a consistent beam of protons with 64.0 MeV. A collimator was placed on the beam such that the effective beam size was approximately that of the Spartan-6 device and no other parts of the mezzanine board received unnecessarily high levels of radiation. This is important because it allows us to be confident that all recorded SEUs were due to a failure of the Spartan-6 FPGA and not from other board components. Note that the other board components have been previously tested and have been shown to be immune to SEUs in the expected HL-LHC radiation environment [48][52].

The Spartan-6 FPGA is programmed with a firmware logic that consists of two pipeline chains, 16-bits wide and 20,000 steps deep (to simulate MPC resource usage), that ran during irradiation. A block diagram of the firmware logic for the pseudo-random bit stream (PRBS) test that was performed can be seen in Figure 4.3. A low-voltage differential signaling cable ( $\sim 8\text{m}$  long) connected the mezzanine board to a Hewlett Packard Agilent 53132A counter to record SEUs. By monitoring the controlled input and the output from the Spartan-6 FPGA SEUs are able to be detected. Only configurable logic blocks (CLB) and flip-flops (FF) were used, which is approximate to realistic MPC firmware, and ran at 40 MHz. All SEUs were recorded, regardless of type. In the case that the SEU caused continuous counting or freezing, a hard reset was manually issued.

#### 4.4 Results

A beam of 64.0 MeV protons was used for all of the irradiation tests of the Xilinx Spartan-6 XC6SLX150T FPGA. Further, all tests were performed on the same Spartan-6 FPGA mounted on the same MPC mezzanine board so that any cumulative effects could be seen.

For the initial test, the Spartan-6 FPGA was irradiated with 1krad at a rate of

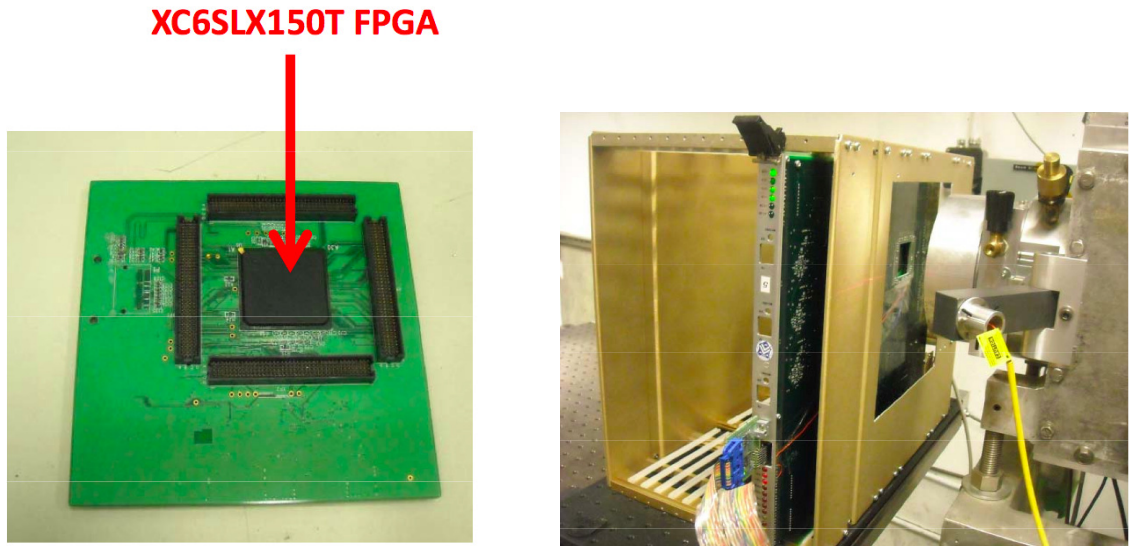


Figure 4.2 : Left picture shows the Xilinx Spartan-6 XC6SLX150T FPGA mounted on the MPC mezzanine board. Right picture shows the mezzanine board held in the crate in the proton beam. [53]

$\sim 1 \frac{\text{rad}}{\text{sec}}$ . This rate was used because it produced a constant rate of SEUs. During this irradiation  $\sim 75$  SEUs were recorded, with an SEU of any type detected every 5-15 seconds with an average dose of  $\sim 13$  rads/SEU. Using the accumulated fluence of  $3 \times 10^{11} \frac{\text{protons}}{\text{cm}^2}$ , the cross section of the SEU is  $2.5 \times 10^{-9} \text{cm}^2$ . Assuming the fluence of  $\sim 10^{11} \frac{\text{neutrons}}{\text{cm}^2}$  (see Table 4.1) for the ME1/1 environment at the HL-LHC design luminosity, the highest potential SEU rate during HL-LHC operation would be 1 SEU every  $\sim 56$  hours per device [47]. Recall that this SEU frequency is inflated because of the overestimated radiation exposure.

The second test was then to determine whether the Spartan-6 FPGA could survive 30krad at a rate of  $80 \frac{\text{rad}}{\text{sec}}$ , the equivalent of 10 years of radiation exposure in the

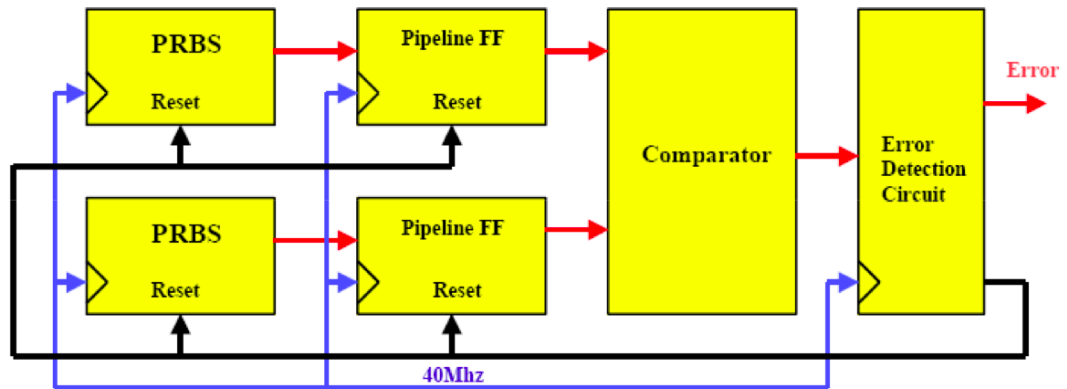


Figure 4.3 : Block diagram of the test design used for the Xilinx Spartan-6 XC6SLX150T FPGA while being irradiated. [53]

ME1/1 area (with a safety factor of 3). As expected, many SEUs of all types were recorded during this test. However, the Spartan-6 FPGA did not lose functionality and was operational throughout the test. To further test the survivability of the Spartan-6 FPGA it was irradiated with 100krad at a rate of  $360 \frac{\text{rad}}{\text{sec}}$ . Once again, there were many SEUs, but the FPGA did not lose functionality throughout the test.

After being irradiated with  $\sim 130\text{krad}$ , the initial test was repeated and the Spartan-6 FPGA was irradiated with  $\sim 300\text{rad}$  at a rate of  $\sim 1 \frac{\text{rad}}{\text{sec}}$  to see if there were any cumulative effects or permanent damage to the FPGA. There were  $\sim 50$  SEUs recorded in 5 minutes, leading to a mean dose of  $\sim 6\text{rads/SEU}$ . Although this is  $\sim 2$  times the SEU rate of the initial test, the FPGA remained fully functional and would therefore only result in 1 SEU every  $\sim 28$  hours per device.

## 4.5 Summary

From the results, the Xilinx Spartan-6 XC6SLX150T FPGA is acceptable for use in the CMS endcap muon environment, and should perform reliably for 10 years of HL-LHC use with an SEU expected every  $\sim 56$  hours per device. These errors may be mitigated by requiring a triple module redundancy (TMR) in the FPGA firmware logic to check for SEUs. Additionally, requiring a periodic reset of all FPGA devices would further reduce potential SEUs. Periodic resets of FPGA devices are currently in effect at the CMS detector. These resets introduce a deadtime of  $\sim 100$ ms every  $\sim 10$ min. The resulting deadtime corresponds to about 0.017% of beam run time, which is negligible and does not affect physics performance. In conjunction, these techniques could effectively make these SEUs negligible.

It is important to note that based on our results, there were minimal cumulative effects on the Spartan-6 FPGA since it was still fully operational after  $\sim 130$ krad. This provides evidence to suggest that there was no significant latchup or other permanent effects that would require hardware replacement during normal HL-LHC operation.

## Chapter 5

### Conclusions and Discussion

#### 5.1 Conclusions

As a result of the irradiation study (presented in Chapter 4), the Xilinx Spartan-6 FPGA will be implemented in the upgraded MPC mezzanine board during LS1 and used in the upgraded CMS detector ( $\sim 2015$ ). This will allow for up to 18 LCTs per MPC to be sent to the the SP, in comparison to the 3 LCTs currently able to be sent. The upgraded MPC mezzanine is expected to be able to function reliably for up to 10 years of HL-LHC use. Additionally, the Spartan-6 FPGA has been used for the upgraded CSC ME1/1 ALCT boards at the CMS detector [54]. It is possible that further hardware applications for the Spartan-6 FPGA will be found at the LHC.

Furthermore, it was found that GMT muon isolation alone is unsuitable for reducing the Level-1 trigger rate in the endcap (presented in Chapter 3). However, a modest form of full granularity isolation as proposed in this study will be included in the upgraded GMT system and used in conjunction with other isolation techniques. Namely, an isolation cut which remains within the plateau region as seen in the ROC plots of Section 3.7 which will allow the rate to be reduced by  $\sim 10\%$  without an ap-

preciable loss of efficiency is recommended. The upgraded MS will therefore include the ability to send muon information to the calorimeter system, allowing GMT muon isolation to be implemented.

## 5.2 Future Work

To fully determine the functionality of GMT muon isolation in the L1 trigger further studies must be completed. This is because the actual effect on the efficiency from GMT muon isolation is not yet clear. Although some isolation cuts were deemed by this study to lower the efficiency by an unacceptable amount, if this efficiency is being lowered by removing events (muons) that would be removed by other processes (such as a higher level trigger) regardless, then the drop in efficiency may be acceptable. Therefore, future studies on investigating the removed muons must be completed in order to determine how higher level procedures would have handled them.

The Level-1 trigger must be able to perform reliably in the upgraded LHC environment. Although GMT muon isolation was not able to sufficiently reduce the rate alone, additional algorithms must be put in place to do so. Without a functioning Level-1 trigger the validity of future physics studies will be compromised. As a last resort, the muon trigger threshold may simply be raised, but interesting physics may be lost.

Another way to reduce the Level-1 trigger rate is to increase the accuracy of muon  $p_T$  assignment [24]. Although increasing the  $p_T$  resolution was not able to improve the capabilities GMT muon isolation adequately, it may be used to stop low  $p_T$  muons from triggering the L1. This might allow the  $p_T$  threshold to remain low while controlling the trigger rate.

Another possible method to reduce the Level-1 trigger rate is by implementing a “track trigger.” Currently, no trigger primitives from the strip and pixel detectors are utilized by the L1; this information is only included in higher level processes. If this information were to be included in the L1, it may allow: better object discrimination (i.e. muons from hadronic activity vs muons from heavy state decays), more accurate  $p_T$  assignment, and better primary vertex finding (allowing discrimination from pile-up) [24].

## References

- [1] Sheldon L. Glashow. Partial-symmetries of weak interactions. *Nuclear Physics*, 22(4):579 – 588, 1961.
- [2] Steven Weinberg. A model of leptons. *Physical Review Letters*, 19(21):1264–1266, 1967.
- [3] A Salam. Elementary particle physics: Relativistic groups and analyticity. In *Proceedings to the Eighth Nobel Symposium*, 1968.
- [4] MissMJ. Standard model of elementary particles. [http://en.wikipedia.org/wiki/Particle\\_physics#mediaviewer/File:Standard\\_Model\\_of\\_Elementary\\_Particles.svg](http://en.wikipedia.org/wiki/Particle_physics#mediaviewer/File:Standard_Model_of_Elementary_Particles.svg).
- [5] D. Griffiths. *Introduction to Elementary Particles*. Physics textbook. Wiley, 2008.
- [6] F. Halzen and A.D. Martin. *Quarks & Leptons: An Introductory Course in Modern Particle Physics*. Wiley India Pvt. Limited, 2008.
- [7] CMS Collaboration. Observation of a new boson at a mass of 125 GeV with the CMS experiment at the LHC. *Phys.Lett.*, B716:30–61, 2012.
- [8] The Particle Physics Project Prioritization Panel (P5). Building for discovery: Strategic plan for u.s. particle physics in the global context. <http://usparticlephysics.org/p5/>, May 2014.
- [9] U.S. Department of Energy. High energy physics (hep): Energy frontier. <http://science.energy.gov/hep/research/energy-frontier/energy-frontier-more-info/>, December 2013.
- [10] L. Silvestris and M. Klute. Status of tp physics studies. <https://indico.cern.ch/event/324714/contribution/1/material/slides/0.pdf>, June 2014.
- [11] CMS Collaboration. Technical proposal for the upgrade of the CMS detector through 2020. Technical Report CERN-LHCC-2011-006. LHCC-P-004, CERN, Geneva, Jun 2011.
- [12] CMS Collaboration. The cms experiment at the cern lhc. *Journal of Instrumentation*, 3:S08004, 2008.

- [13] CMS Collaboration. Cms physics technical design report volume i: Detector performance and software. technical design report cms. cern, geneva. Technical report, CMS-TDR-008-1, 2006.
- [14] G.L. Bayatian et al. CMS technical design report, volume II: Physics performance. *J.Phys.*, G34:995–1579, 2007.
- [15] CMS Collaboration. Cms luminosity - public results. <https://twiki.cern.ch/twiki/bin/view/CMSPublic/LumiPublicResults>.
- [16] Jay Hauser. Physics of the high luminosity lhc upgrade. Seminar, March 2014.
- [17] Dylan Gilbert. Informal lectures and seminar on particle physics 2013. <http://www.t2.ucsd.edu/twiki2/bin/view/UCSDTier2/ParticlePhysics2013>, December 2013.
- [18] Brian Martin. *Nuclear and Particle Physics: An Introduction*. John Wiley & Sons, Ltd, 2009.
- [19] Breedon R, Cox T, Ko W, Hauser J, M. von der Mey, Bondar N, Ferguson T, Vorobiev I, Karjavin V, Khabarov S, Acosta D, Madorsky A, Mitselmakher G, Korytov A, Apollinari G, Borcharding F, Geurts F, Prokofiev O, Lusin S, Bylsma B, Durkin S, Gilmore J, Ling T.Y., Matveev M, P Padley, Tumanov A, Golyash A, Uvarov L, and Loveless R. Csc strip, wire, chamber, and electronics conventions. *Internal Note*, Mar 2007.
- [20] CMS Collaboration. CMS, the Compact Muon Solenoid. Muon technical design report. 1997.
- [21] J. Hauser, D. Acosta, E. Boyd, B. Bylsma, R. Cousins, A. Drozdetski, S. Durkin, J. Gilmore, J. Gu, S. Haapanen, A. Korytov, S. Lee, T. Ling, A. Madorsky, M. Matveev, M. Mey, B. Mohr, J. Mumford, P. Padley, G. Pawloski, J. Roberts, B. Scurlock, H. Stoeck, V. Valuev, G. Veramendi, J. Werner, and Y. Zheng. Experience with trigger electronics for the csc system of cms. *10th Workshop on Electronics for LHC and Future Experiments, Boston, MA, USA, 13 - 17 Sep 2004*, pp.292-297, 2004.
- [22] M.M. Baarmand, A. Vanyashin, Yu. Bonushkin, C. Matthey, J. Hauser, et al. Spatial resolution attainable with cathode strip chambers at the trigger level. *Nucl.Instrum.Meth.*, A425:92–105, 1999.
- [23] K Ecklund, J Liu, A Madorsky, M Matveev, and P Padley. Upgrade of the cathode strip chamber level 1 trigger optical links at cms. *Journal of Instrumentation*, 7(11):C11011, 2012.

- [24] CMS Collaboration. Cms technical design report for the level-1 trigger upgrade. Technical report, CERN, 2013.
- [25] M. Matveev and P. Padley. Upgrade of the csc endcap muon port card at cms. *Journal of Instrumentation*, 5:C11013, 2010.
- [26] J Rorie. Csc data flow. Personal Correspondence, May 2014.
- [27] D Acosta, G P Di Giovanni, D Holmes, A Madorsky, M Matveev, P Padley, L Redjimi, L Uvarov, and D Wang. Commissioning of the csc level 1 trigger optical links at cms. *Topical Workshop on Electronics for Particle Physics, Paris, France, 21 - 25 Sep 2009, pp.431-434*, 2009.
- [28] CMS Collaboration. Cms tridas project: Technical design report, volume 1: The trigger systems. Technical report, CERN, 2000.
- [29] CMS Collaboration. Performance of the cms drift tube chambers with cosmic rays. *Journal of Instrumentation*, 5(03):T03015, 2010.
- [30] Lucas Taylor. Muon drift tubes. <http://cms.web.cern.ch/news/muon-drift-tubes>, Noveber 2011.
- [31] Filip Thyssen. Performance of the resistive plate chambers in the cms experiment. *Journal of Instrumentation*, 7(01):C01104, 2012.
- [32] Lucas Taylor. Resistive plate chambers. <http://cms.web.cern.ch/news/resistive-plate-chambers>.
- [33] Wesley Smith. Triggering cms. Texas A & M Seminar: Triggering CMS, April 2011.
- [34] J Lingemann H Sakulin, D Rabady. ugmt status and plans. In *L1 Muon Trigger upgrade meeting*. CMS, May 2014.
- [35] CMS Collaboration. Invariant-mass spectra of opposite-sign muon pairs. <https://twiki.cern.ch/twiki/bin/view/CMSPublic/PhysicsResultsMU0>, October 2011.
- [36] Michael Leyton and on behalf of the ATLAS Collaboration. Minimum bias and underlying event measurements with atlas. <http://arxiv.org/abs/1202.2090>, 02 2012.
- [37] Slhcupgradesimulations. <https://cmsdt.cern.ch/SDT/lxr/source/SLHCUpgradeSimulations/>, 2014.
- [38] Sridhara Dasu. Regional calorimeter trigger. <http://www.hep.wisc.edu/cms/trig/RCTReview.html>, September 2003.

- [39] Tpg to rct mapping information. <http://www.hep.wisc.edu/cms/trig/calorimeter-mapping.html>.
- [40] Muon analysis. [https://twiki.cern.ch/twiki/bin/view/CMSPublic/WorkBookMuonAnalysis#Global\\_muons](https://twiki.cern.ch/twiki/bin/view/CMSPublic/WorkBookMuonAnalysis#Global_muons), March 2009.
- [41] CMS Collaboration. Baseline muon selections. <https://twiki.cern.ch/twiki/bin/view/CMSPublic/SWGuideMuonId>, January 2014.
- [42] Particle flow. <https://twiki.cern.ch/twiki/bin/view/CMSPublic/SWGuideParticleFlow>, October 2011.
- [43] M. Mulders, I. Bloch, E. James, A. Everett, D. Barge, C. Campagnari, P. Kalavase, V. Krutelyov, D. Kovalskyi, J. Ribnik, and N. Amapane. Muon identification in cms. *Analysis Note*, CMS AN-2008/098, 2008.
- [44] Ivan Mikulec. Changes in the global muon trigger configuration during data taking. <https://twiki.cern.ch/twiki/bin/viewauth/CMS/GlobalMuonTriggerChanges>, October 2011.
- [45] Jim Brooke. Global muon trigger emulation twiki. <https://twiki.cern.ch/twiki/bin/view/CMSPublic/SWGuideL1GMTEmulator?redirectedfrom=CMS.SWGuideL1GMTEmulator>, June 2008.
- [46] M Matveev. Csc endcap muon port card and muon sorter upgrade status. US CMS Endcap Muon Collaboration Meeting, TAMU. [http://bonner-ntserver.rice.edu/cms/MPC\\_MS\\_upgrade\\_05\\_2013.pdf](http://bonner-ntserver.rice.edu/cms/MPC_MS_upgrade_05_2013.pdf), September 2013.
- [47] M. Huhtinen. Cms cots workshop. <https://twiki.cern.ch/twiki/pub/Sandbox/RadiationHardCOTS/CMStutorial1.pdf>, November 1999.
- [48] B. Bylsma, D. Cady, A. Celik, L. S. Durkin, J. Gilmore, J. Haley, V. Khotilovich, S. Lakdawala, J. Liu, M. Matveev, B. P. Padley, J. Roberts, J. Roe, A. Safonov, I. Suarez, D. Wood, and I. Zawisza. Radiation testing of electronics for the cms endcap muon system. *Nuclear Instruments & Methods In Physics Research Section A-Accelerators Spectrometers Detectors and Associated Equipment*, 698:242–248, 2013.
- [49] M. Matveev et al. Irradiation test of the altera programmable devices at the cms muon endcap clock and control board. <http://bonner-ntserver.rice.edu/cms/altera.pdf>, 2002.
- [50] M Huhtinen and F Faccio. Computational method to estimate single event upset rates in an accelerator environment. *Nuclear Instruments & Methods In Physics Research Section A-Accelerators Spectrometers Detectors and Associated Equipment*, 450:155–172, 2000.

- [51] F. Faccio. Cots for the lhc radiation environment: the rules of the game. In *Presented at the 6th Workshop on Electronics for LHC Experiments*, Krakow, Poland, 2000.
- [52] M. Matveev et al. Optical link evaluation for the csc muon trigger at cms. In *Proceedings of the Seventh Workshop on Electronics for LHC Experiments*, volume 034, pages 379–382. CERN/LHCC, Stockholm Sweden, September 2001.
- [53] P Padley. Irradiation test of the spartan-6 muon port card mezzanine. [http://bonner-ntserver.rice.edu/cms/mpc\\_irr\\_0413.pdf](http://bonner-ntserver.rice.edu/cms/mpc_irr_0413.pdf), April 2013.
- [54] Hauser J. Proposed alct replacement. <https://indico.cern.ch/event/200865/material/slides/1?contribId=4>, July 2012.